Journal Pre-proof

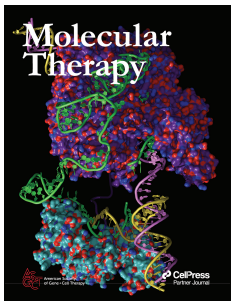

AAV-mediated CBLN1 replacement rescues hereditary ataxia caused by biallelic *CBLN1* variants

Tokiwa Yamasak, Wataru Kakegawa, Ayumi Hayashi, Naoko Ogawa, Tetsuya Takano, Keiko Matsuda, Kumi Takatsuto, Mohamed S. Abdel-Hamid, Maha S. Zaki, Joseph Gleeson, Michisuke Yuzaki

PII: S1525-0016(26)00772-0

DOI: https://doi.org/10.1016/j.ymthe.2026.09.003

Reference: YMTHE 7713

To appear in: *Molecular Therapy*

Received Date: 21 April 2026

Accepted Date: 1 September 2026

Please cite this article as: Yamasak T, Kakegawa W, Hayashi A, Ogawa N, Takano T, Matsuda K, Takatsuto K, Abdel-Hamid MS, Zaki MS, Gleeson J, Yuzaki M, AAV-mediated CBLN1 replacement rescues hereditary ataxia caused by biallelic *CBLN1* variants, *Molecular Therapy* (2026), doi: https://doi.org/10.1016/j.ymthe.2026.09.003.

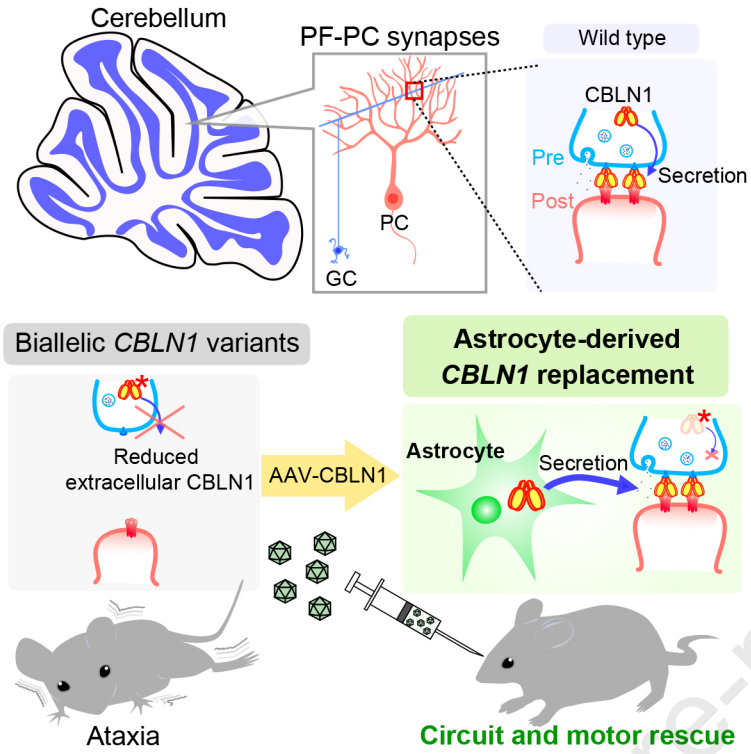

AAV-mediated CBLN1 replacement rescues hereditary ataxia caused by biallelic *CBLN1* variants

Tokiwa Yamasak[1,7], Wataru Kakegawa[1,2,3,7], Ayumi Hayashi[1,2], Naoko Ogawa[1,2], Tetsuya Takano[1], Keiko Matsuda[1,2], Kumi Takatsuto[1], Mohamed S. Abdel-Hamid[4], Maha S. Zaki[5], Joseph Gleeson[6], Michisuke Yuzaki[1,2,8]

[1]Department of Physiology, Keio University School of Medicine, Tokyo 160-8582, Japan.
[2]Center for Human Biology-Microbiota-Quantum Computational Research, Keio University, Tokyo 160-8582, Japan.
[3]Department of Life Sciences, Faculty of Science, Gakushuin University, Tokyo 171-8588, Japan.
[4]Medical Molecular Genetics Department, Human Genetics and Genome Research Institute, National Research Center, Cairo 12622, Egypt.
[5]Clinical Genetics Department, Human Genetics and Genome Research Institute, National Research Center, Cairo 12622, Egypt.
[6]Rady Children's Institute for Genomic Medicine, University of California San Diego, La Jolla, CA 92093, USA.
[7]These authors contributed equally.
[8]Lead Contact

*Correspondence: myuzaki@keio.jp (M.Y.)

Abstract

Cbln1 is a secreted synaptic organizer required for parallel fiber–Purkinje cell (PF–PC) synapse integrity, climbing fiber (CF) refinement, and cerebellar motor learning, but has not previously been implicated in human disease. We identified biallelic *CBLN1* missense variants (A63P and Y112C) in two unrelated families with early-onset cerebellar ataxia accompanied by oculomotor abnormalities, cerebellar atrophy, and variable cognitive delay. In heterologous cells, both variants showed reduced steady-state protein abundance, impaired maturation through the early secretory pathway, and little or no detectable secretion, resulting in markedly reduced extracellular CBLN1 availability. Consistently, cerebellar granule cells expressing CBLN1-Y112C failed to induce excitatory synapses onto glutamate receptor δ2 (GluD2)-expressing cells *in vitro*. A knock-in mouse harboring Y112C lacked synaptic Cbln1 and recapitulated key features of Cbln1 deficiency, including disrupted PF–PC synapse organization, persistent CF multi-innervation, impaired PF–PC transmission and long-term depression, and deficits in motor coordination and oculomotor learning. Notably, systemic delivery of an astrocyte-targeted adeno-associated virus expressing wild-type CBLN1 in adult mutant mice restored synaptic CBLN1 localization, cerebellar synaptic function, plasticity, and behavior. These findings establish CBLN1 deficiency as a cause of hereditary ataxia and identify extracellular CBLN1 replacement as a therapeutic strategy for a reversible cerebellar synaptopathy.

INTRODUCTION

Hereditary cerebellar ataxias are clinically and genetically heterogeneous disorders characterized by gait and limb incoordination, dysarthria, and oculomotor abnormalities, often beginning in infancy or childhood.[1,2] Although genomic sequencing has expanded the catalog of ataxia genes, many familial cases remain unexplained, and disease-modifying therapies are limited.[3] Increasing evidence suggests that defective synapse assembly, maintenance, or refinement—so-called synaptopathy—is a convergent mechanism across a broad range of neurodevelopmental and

neurological disorders, including several cerebellar ataxias.[4] Identifying molecular determinants of cerebellar synapse integrity is therefore important not only for disease gene discovery but also for the development of mechanistically targeted therapies.

In the cerebellum, parallel fiber–Purkinje cell (PF–PC) synapses provide the major excitatory input to Purkinje cells and support motor learning through activity-dependent plasticity. These synapses are organized by extracellular molecules that align pre- and postsynaptic compartments. Among these, CBLN1,[5] a secreted C1q family glycoprotein released from granule cell axons,[6] forms a trans-synaptic complex with presynaptic neurexins and postsynaptic glutamate receptor δ2 (GluD2; encoded by *GRID2*),[7–9] thereby promoting PF–PC synapse formation and long-term stabilization.[10,11] *Cbln1* knockout mice show reduced PF–PC synapse number, impaired excitatory transmission, and defective long-term depression (LTD), a form of synaptic plasticity essential for cerebellar motor learning, including optokinetic response (OKR) adaptation.[12,13] Reduced PF input also disrupts developmental elimination of surplus climbing fiber (CF) inputs, resulting in persistent multiple CF innervation of Purkinje cells.[12] Together, these findings establish Cbln1 as a central extracellular organizer of cerebellar circuit maturation, plasticity, and maintenance. However, whether CBLN1 dysfunction causes human cerebellar disease, and whether restoration of extracellular CBLN1 can rescue circuit dysfunction in adulthood, have remained unknown.[14,15]

Here, we identify biallelic missense variants in *CBLN1* in two unrelated families with early-onset cerebellar ataxia accompanied by prominent oculomotor abnormalities and progressive cerebellar atrophy. We show that both variants impair intracellular trafficking and secretion, markedly reducing extracellular CBLN1 availability. A knock-in mouse carrying the patient-derived Y112C variant recapitulates synaptic, circuit, electrophysiologic, and behavioral features of Cbln1 deficiency. Finally, we demonstrate that systemic delivery of an astrocyte-targeted adeno-associated virus (AAV) expressing wild-type CBLN1 in adult mutant mice restores PF–PC synaptic integrity, CF mono-innervation, LTD, and motor and oculomotor function. These

findings establish CBLN1 deficiency as a cause of hereditary ataxia and identify extracellular CBLN1 replacement as a therapeutic strategy for a reversible cerebellar synaptopathy.

RESULTS

Biallelic CBLN1 missense variants segregate with early-onset cerebellar ataxia

We identified two consanguineous Egyptian pedigrees (families 1613 and 24661) in which affected children presented with early-onset neurologic features consistent with cerebellar dysfunction (Figure 1A; Table 1). In both families, the unaffected parents were first cousins. Symptoms became apparent at 3–4 months of age, initially as abnormal eye movements and delayed motor milestones. Oculomotor abnormalities included tonic upgaze, strabismus, and horizontal nystagmus; tonic upgaze partially improved with age. All affected individuals subsequently developed truncal and appendicular ataxia, hypotonia, and progressive gait impairment. At the most recent evaluation, patient 1, the oldest affected individual (16 years), could walk only a few unsupported steps, whereas patients 2 and 3 required assistance for ambulation. Limb ataxia was evident on finger-to-nose testing. Brain MRI showed cerebellar atrophy, most prominent in the vermis in patients 1 and 2 and progressive in patient 3 (Figures 1B, S1A, and S1B). Together, these findings define an early-onset cerebellar syndrome characterized by prominent oculomotor abnormalities and progressive cerebellar atrophy.

In addition to motor features, affected individuals showed mild-to-moderate neurocognitive impairment (Table 1). Language development was delayed, with first words emerging at 18–24 months and two-word sentences at 3–5 years of age. All patients were able to follow instructions; the two older individuals recognized letters, numbers, and words, whereas the youngest recognized body parts and a limited set of colors and objects. IQ values were approximately 70. This clinical constellation—ataxia, abnormal oculomotor control, cerebellar atrophy, and cognitive delay—resembles phenotypes reported in disorders affecting the PF–PC synaptic organizer pathway, including patients with *GRID2* variants[16–20] and *Cbln1*-null[12] or *Grid2*-null[21,22]

mice. Additional findings, including dysmorphic facies, myopia, and a thin corpus callosum, were also present (Table 1), suggesting that the clinical spectrum may not be limited to cerebellar dysfunction alone.

Genomic sequencing identified missense variants in *CBLN1*: c.187G>C (p.A63P) in family 24661 and c.335A>G (p.Y112C) in family 1613 (Figure 1C). In each family, affected individuals were homozygous for the respective variant, consistent with autosomal recessive inheritance. In family 1613, Sanger sequencing confirmed segregation of c.335A>G, with parental samples showing overlapping A/G peaks at the variant position and affected individuals showing a single G peak (Figure 1D). Likewise, in family 24661, c.187G>C segregated with disease, with parental samples showing overlapping G/C peaks and the affected individual showing a single C peak at the variant position (Figure 1E). These data support autosomal recessive inheritance of both alleles.

Because Cbln1 is a secreted synaptic organizer[6] that bridges presynaptic neurexins and postsynaptic GluD2[7,8] to establish and maintain PF–PC synapses,[10,11] we hypothesized that these variants reduce extracellular CBLN1 availability and thereby impair cerebellar synapse integrity and circuit refinement. To test this hypothesis, we examined the cellular consequences of the variants, generated an *in vivo* knock-in model, and evaluated an AAV-mediated replacement strategy.

Patient-derived *CBLN1* variants show reduced protein abundance, impaired forward trafficking, and defective secretion

CBLN1 assembles as a dimer of trimers, and proper trimerization depends on the globular C1q domain shared by C1q family proteins (Figure 2A).[23] Structural mapping onto the CBLN1 C1q domain (PDB: 5KC5) placed A63 (βA) and Y112 (βC) near the subunit contact surface within the trimer,[24] raising the possibility that these substitutions destabilize oligomerization and thereby affect protein stability, intracellular trafficking, and secretion (Figure 2B). To test this, we

expressed HA-tagged wild-type CBLN1 (CBLN1-WT) or the patient-derived variants (CBLN1-A63P and CBLN1-Y112C) in HEK293 cells and quantified protein in cell lysates and conditioned media. CBLN1-WT was readily detected in both lysates and media in a DNA dose-dependent manner, consistent with efficient secretion. In contrast, both CBLN1-A63P and CBLN1-Y112C reduced intracellular abundance and were not detected in conditioned media, indicating markedly reduced steady-state protein abundance together with a severe secretion defect (Figure 2C).

Co-expression experiments further showed that CBLN1-A63P and CBLN1-Y112C reduced the amount of secreted CBLN1-WT in this heterologous system. Conversely, co-expression of CBLN1-WT partially restored secretion of CBLN1-A63P and CBLN1-Y112C (Figures S2A and S2B), consistent with heteromer formation. Thus, both patient-derived variants markedly reduce extracellular CBLN1 availability and can influence wild-type CBLN1 trafficking when co-expressed *in vitro*.

We next asked whether the secretion defect reflected impaired trafficking through the secretory pathway. PNGase F treatment reduced the apparent molecular weight of both wild-type and mutant proteins, indicating N-glycosylation (Figure 2D). Notably, CBLN1-WT contained an Endo H-resistant fraction, consistent with maturation beyond the endoplasmic reticulum (ER)/cis-Golgi.[25] By contrast, Endo H-resistant species were markedly reduced for CBLN1-A63P and CBLN1-Y112C (Figure 2D), indicating impaired maturation and retention within early secretory compartments. These glycosylation profiles support defective forward trafficking as a major contributor to the reduced extracellular availability of the mutant proteins.

Because CBLN1 acts extracellularly by binding the amino-terminal domain (ATD) of GluD2 on Purkinje cells to organize PF–PC synapses,[7,24] a secretion-defective variant would be expected to be functionally compromised at the synaptic level. We tested this prediction using an artificial synapse-formation assay in which cerebellar granule cells induce presynaptic differentiation on HEK293 cells expressing the GluD2-ATD. As expected, vesicular glutamate transporter 1 (vGluT1) accumulated around HEK293 cells co-cultured with wild-type granule cells but not

around those co-cultured with *Cbln1*-null granule cells, confirming Cbln1 dependence (Figure 2E). Re-expression of CBLN1-WT in *Cbln1*-null granule cells restored vGluT1 accumulation, whereas expression of CBLN1-Y112C did not (Figure 2E). These results indicate that CBLN1-Y112C fails to support CBLN1-dependent excitatory synapse organization *in vitro*, consistent with loss of extracellular CBLN1 availability.

A *Cbln1*$^{Y112C/Y112C}$ knock-in mouse lacks synaptic Cbln1 and recapitulates cerebellar motor and oculomotor phenotypes

To model the disease mechanism *in vivo*, we generated a knock-in mouse carrying the Y112C substitution in the endogenous *Cbln1* locus (Figure 3A). Homozygous *Cbln1*$^{Y112C/Y112C}$ mice were obtained at Mendelian ratios (WT:heterozygous:homozygous = 42:95:42 among 179 pups), indicating no major embryonic lethality. Gross cerebellar foliation and lamination were preserved, but cerebellar size was reduced (Figure 3B). Quantification of the vermal cross-sectional area revealed an approximately 28% reduction in *Cbln1*$^{Y112C/Y112C}$ mice compared with wild-type mice (3.3 versus 4.6 mm^2), paralleling the cerebellar atrophy observed in affected individuals. Because the molecular layer was also substantially reduced in size, we assessed Purkinje cell dendritic processes using both dendritic length density (Car8-positive skeletonized dendritic length per unit molecular layer area) and an estimate of total dendritic length across the molecular layer. Dendritic length density was not significantly different between genotypes and tended to be higher in mutant mice, potentially reflecting denser packing of dendritic processes within the smaller molecular layer. We therefore calculated the estimated total Car8-positive dendritic length by multiplying dendritic length density by molecular layer area. This value was significantly reduced in *Cbln1*$^{Y112C/Y112C}$ mice (Figure S3A). Thus, the knock-in model reproduces a structural cerebellar abnormality without overt defects in foliation or lamination, permitting circuit-level analysis.

We next asked whether synaptic Cbln1 was present in the mutant cerebellum. After pepsin pretreatment to enhance detection of synaptic proteins,[26] the wild-type cerebellar cortex showed

183 punctate Cbln1 immunoreactivity colocalized with GluD2. By contrast, synaptic Cbln1
184 immunoreactivity was essentially absent in the *Cbln1*$^{Y112C/Y112C}$ cerebellum, closely resembling
185 *Cbln1*-null tissue (Figures 3C and S4A). These data indicate that the Y112C substitution
186 effectively abolishes synaptic Cbln1 *in vivo*, consistent with markedly reduced extracellular
187 Cbln1 availability.

188 Behavioral analyses demonstrated robust cerebellar dysfunction in *Cbln1*$^{Y112C/Y112C}$ mice.
189 Mutant mice exhibited tremor and marked gait instability in the open field (Movie S1) and fell
190 within seconds on the rotarod at 20 rpm (Figure 3D). Treadmill gait analysis showed increased
191 maximal toe height, indicative of abnormal hindlimb coordination, as previously reported in
192 *Cbln1*-null mice (Figure 3E). Finally, video-oculography revealed abnormally large spontaneous
193 eye movements in mutant mice (Figure 3F), mirroring the prominent oculomotor abnormalities
194 observed in the affected individuals. Thus, *Cbln1*$^{Y112C/Y112C}$ mice reproduce key motor and
195 oculomotor features of the human disorder and provide a tractable model for mechanistic and
196 therapeutic studies.

197

198 **Cbln1-Y112C disrupts PF–PC synapse organization and impairs CF refinement**

199 We next examined whether Cbln1-Y112C disrupts PF–PC synapse organization, a hallmark of
200 Cbln1 deficiency. In both wild-type and *Cbln1*$^{Y112C/Y112C}$ cerebella, vGluT1-labeled PF terminals
201 and GluD2-labeled postsynaptic sites showed punctate patterns. In mutant tissue, however, these
202 puncta were less sharply demarcated and more diffuse. Consistent with this altered distribution,
203 pixel intensity-based correlation between vGluT1 and GluD2 immunoreactivity was reduced
204 (Figures 4A and 4B), similar to that observed in *Cbln1*-null mice (Figure S4B). Because this
205 metric is sensitive to signal spread and reduced compartmentalization, the result is consistent with
206 impaired pre- and postsynaptic alignment and with the presence of uninnervated ("naked")
207 Purkinje cell spines previously described in *Cbln1*-null mice.[12] Further analysis of the presynaptic
208 compartment revealed that, despite a reduction in the number of vGluT1-positive puncta, the

remaining puncta were larger and showed increased vGluT1 signal intensity (Figure S3B), a pattern also reported in *Cbln1-null* mice.[27] These findings indicate that loss of synaptic Cbln1 in the knock-in cerebellum is associated with structural disruption and remodeling of PF–PC synapse organization.

We then examined PF–PC synaptic function. Whole-cell recordings from Purkinje cells in acute cerebellar slices showed that PF-evoked excitatory postsynaptic current (EPSC) amplitudes were significantly reduced in mutant mice (Figure 4C). Paired-pulse facilitation was increased (Figure 4D), indicating a lower presynaptic release probability. Thus, PF–PC synaptic transmission is functionally compromised in *Cbln1*$^{Y112C/Y112C}$ mice.

Because PF–PC synapse defects are known to impair developmental refinement of CF inputs,[28,29] we next analyzed CF territory and innervation state. In wild-type animals, vGluT2-positive CF terminals were restricted to proximal dendritic regions, whereas vGluT1-positive PF terminals predominated in distal spiny branchlets.[30] In *Cbln1*$^{Y112C/Y112C}$ cerebellum, vGluT2 puncta extended significantly farther into the molecular layer (Figure 4E), indicating abnormal expansion of CF territory into the PF domain. We then estimated the number of functional CF inputs onto individual Purkinje cells by recording CF-evoked EPSCs across a range of stimulus intensities (Figure 4F). Many mutant Purkinje cells showed multistep CF-EPSC responses, indicative of persistent multiple CF innervation (Figure 4G). In addition, the amplitude of the strongest CF-EPSC was reduced in mutant Purkinje cells relative to wild type (Figure 4H), consistent with impaired developmental strengthening and pruning of CF inputs.[28] Together, these data show that Cbln1-Y112C disrupts PF–PC synapse organization and is accompanied by defective restriction of CF territory and failure of CF mono-innervation.

PF–PC LTD and cerebellar motor learning are severely impaired in *Cbln1*$^{Y112C/Y112C}$ mice

At PF–PC synapses, CF activity provides a teaching signal that, when paired with PF input, induces LTD of subsequent PF–PC synaptic transmission.[13] Because PF–PC LTD is a canonical

form of cerebellar synaptic plasticity linked to motor learning, we asked whether it is altered in *Cbln1*$^{Y112C/Y112C}$ mice. In wild-type slices, conjunctive PF stimulation paired with Purkinje cell depolarization, used as a surrogate for CF activation, induced robust LTD, reflected by a sustained reduction in PF-evoked EPSC amplitude. In contrast, the same induction protocol failed to depress PF-EPSCs in mutant slices (Figures 5A–5C). These results indicate that Cbln1-Y112C disrupts a canonical form of PF–PC synaptic plasticity required for cerebellar learning.

We next examined cerebellum-dependent motor learning using adaptation of the horizontal optokinetic response (hOKR). Repetitive horizontal motion of a checkerboard screen increased hOKR gain in wild-type mice, but not in *Cbln1*$^{Y112C/Y112C}$ mice, over 60 min of training (Figures 5D and 5E). Thus, the PF–PC plasticity defect in *Cbln1*$^{Y112C/Y112C}$ mice is accompanied by impaired cerebellar motor learning *in vivo*.

Astrocyte-targeted gene delivery restores synaptic Cbln1 in the adult mutant cerebellum

Previous studies showed that recombinant Cbln1 protein delivered into the subarachnoid space over the cerebellum can acutely rescue phenotypes in *Cbln1*-null mice, although the effect is transient and lasts approximately 1 week.[10,31] To determine whether recombinant Cbln1 could similarly rescue the patient-derived mutant phenotype, we applied the same approach to *Cbln1*$^{Y112C/Y112C}$ mice and longitudinally evaluated motor performance using the rotarod test. Recombinant Cbln1 significantly improved motor performance on days 3–5 after injection, with the maximal effect observed on day 4 (Figure S5). The improvement subsequently declined and was no longer statistically significant at the group level after day 8; by 3 weeks after injection, performance had returned to approximately pre-treatment levels. These results confirm that extracellular Cbln1 replacement can functionally rescue the Y112C mutant phenotype, but also demonstrate the transient nature of protein-based replacement. We therefore sought a strategy that could provide sustained extracellular CBLN1 availability.

To express CBLN1 in granule cells, the endogenous source of Cbln1, we first packaged a

CBLN1 expression cassette driven by a $GABA_A$ receptor α6 (*Gabra6*) promoter[32] in an AAV vector and injected it directly into the cerebellum (Figure S6A). Two weeks later, immunoblotting and immunohistochemistry showed little or no detectable GFP or HA-CBLN1 expression (Figures S6B and S6C), indicating that this promoter configuration was insufficient for robust expression in mature granule cells *in vivo*.

We therefore turned to astrocytes as an alternative source of CBLN1. Astrocytes are closely apposed to PF–PC synapses in the molecular layer,[33] and extracellular Cbln1 can in principle be captured at these synapses through its binding to neurexins and GluD2. After direct cerebellar injection of an AAV vector encoding HA-CBLN1 under the astrocyte-specific *GfaABC1D* promoter,[34] robust GFP and HA-CBLN1 expression was detected in cerebellar lysates (Figures S6A and S6B). By immunohistochemistry, GFP signal was observed in Bergmann glia and granule layer astrocytes, whereas HA-CBLN1 signal was prominent in the molecular layer, where PF–PC synapses reside (Figure S6C). This pattern is consistent with astrocytic expression followed by secretion and synaptic capture of CBLN1.

To test therapeutic potential, we next delivered the astrocyte-targeted vector systemically by retro-orbital injection into adult *Cbln1*$^{Y112C/Y112C}$ mice (Figure 6A). Immunohistochemistry showed widespread cerebellar transduction (Figure S6D). GFP signal colocalized with S100β-positive astrocytes, whereas HA signal was concentrated in the molecular layer irrespective of S100β immunoreactivity, again consistent with secretion and extracellular distribution of CBLN1 (Figures S6E and S6F). Importantly, pepsin-assisted synaptic staining revealed reappearance of punctate HA-CBLN1 signals colocalized with GluD2, indicating restoration of synaptic CBLN1 at PF–PC synapses (Figure 6B). These findings show that systemic astrocyte-targeted gene delivery restores synaptic localization of CBLN1 in the adult mutant cerebellum. Systemic delivery also resulted in broad HA-CBLN1 expression in extracerebellar regions, including the hippocampus and cerebral cortex, with a distribution that differed from that of endogenous Cbln1 in HA-Cbln1 knock-in mice (Figures S7A–S7C).

Astrocyte-targeted AAV rescues synaptic, circuit, and behavioral phenotypes in adult *Cbln1*$^{Y112C/Y112C}$ mice

We next asked whether astrocyte-derived CBLN1 restores PF–PC synapse organization and function. Car8-positive dendritic length density was also significantly increased after HA-CBLN1 expression. Accordingly, the estimated total Car8-positive dendritic length across the molecular layer, calculated as dendritic length density multiplied by molecular layer area, was significantly increased in HA-CBLN1-treated mutant mice (Figure S8B). These findings indicate recovery of structural measures of the Purkinje cell dendritic compartment. Immunostaining for vGluT1 and GluD2 showed improved pre- and postsynaptic alignment in rescue-treated mutant mice (Figure 6C). Similarly, the reduced number of vGluT1 puncta was increased, whereas the increased size and intensity of the remaining vGluT1 puncta were reduced toward wild-type levels by expression of HA-CBLN1 in *Cbln1*$^{Y112C/Y112C}$ mice (Figure S8C). Whole-cell recordings further demonstrated normalization of PF-EPSC amplitudes and reduction of paired-pulse facilitation toward wild-type values (Figure 6D), indicating recovery of PF–PC synaptic transmission. To assess whether astrocyte transduction altered endogenous astrocyte function, we examined glutamate uptake using the astrocytic glutamate transporter inhibitor TFB-TBOA.[35] The effects of TFB-TBOA on PF-EPSC amplitude and kinetics were not detectably altered by astrocyte transduction (Figure S9), arguing against a major change in astrocyte-dependent glutamate clearance under these conditions. Thus, astrocyte-derived CBLN1 is sufficient to restore PF–PC synapse organization and transmission without evidence that the rescue is mediated by altered astrocyte glutamate handling.

Rescue treatment also corrected CF abnormalities. The distribution of vGluT2-positive terminals in the molecular layer shifted toward the wild-type pattern (Figures S8D and S8E), and multistep CF-EPSC responses were markedly reduced, indicating restoration of CF mono-innervation (Figure 6E). In addition, the amplitude of the strongest CF-EPSC recovered toward

wild-type levels (Figure 6F). These findings indicate that extracellular CBLN1 replacement is sufficient to restore key features of CF refinement.

We then asked whether the rescue strategy restores synaptic plasticity and motor learning. Conjunctive stimulation robustly induced PF–PC LTD in slices from rescue-treated *Cbln1*$^{Y112C/Y112C}$ mice, whereas control-treated mutant slices remained LTD-deficient (Figure 6G). At the behavioral level, rescue-treated mutants regained hOKR adaptation, showing a significant increase in gain after training (Figure 6H). Rescue-treated mice also no longer displayed prominent tremor or gait instability (Movie S2). Rotarod and treadmill performance improved markedly, reaching near-wild-type levels (Figures 6I and S8F), and abnormal spontaneous eye movements were normalized (Figure 6J). Behavioral improvements were quantitatively demonstrated 1–2 months after injection, and improved spontaneous locomotion remained evident qualitatively at 6 months (Movie S3). Together, these findings show that AAV-mediated extracellular CBLN1 replacement reverses multiple features of cerebellar synaptopathy, spanning structural abnormalities, synapse organization, circuit refinement, synaptic plasticity, and behavior.

DISCUSSION

In this study, we provide convergent human genetic, mechanistic, and therapeutic evidence that biallelic CBLN1 variants cause an early-onset cerebellar disorder characterized by ataxia, oculomotor abnormalities, cerebellar atrophy, and variable cognitive delay. Mechanistically, these variants show reduced steady-state protein abundance together with severely impaired forward trafficking and secretion, resulting in marked reduction of extracellular CBLN1 availability and loss of synapse-organizing activity *in vitro*. We further establish a *Cbln1*$^{Y112C/Y112C}$ knock-in model that lacks synaptic Cbln1 and recapitulates core cerebellar circuit abnormalities associated with Cbln1 deficiency, including impaired PF–PC synapse integrity, defective CF refinement, loss of PF–PC LTD, and deficits in cerebellar motor learning. Finally, we show that

systemic delivery of an astrocyte-targeted AAV expressing wild-type CBLN1 restores synaptic CBLN1 localization and reverses abnormalities spanning synaptic structure, transmission, plasticity, and behavior. Together, these findings establish CBLN1 deficiency as a cause of human cerebellar synaptopathy and identify extracellular CBLN1 replacement as a therapeutic strategy.

CBLN1-dependent cerebellar synapse biology extends to human disease

Cbln1 is a secreted synaptic organizer that forms a transsynaptic complex with presynaptic neurexins and postsynaptic GluD2 at PF–PC synapses.[7,8] In rodents, deletion of Cbln1 or GluD2 causes strikingly convergent phenotypes, including marked loss of PF–PC synapses, impaired PF transmission and LTD, and abnormal CF territory and mono-innervation.[12,21] Although human GluD2-related disorders support conservation of GluD2 function in cerebellar circuit development,[16–20] whether CBLN1 plays an analogous role in humans has remained uncertain because no previously reported CBLN1 variants have been established as pathogenic through functional and *in vivo* validation.[15,36]. The affected individuals described here show a phenotype fully consistent with disruption of the GluD2–CBLN1 pathway, and our cellular and *in vivo* data provide direct mechanistic evidence that disruption of this pathway causes human disease. Thus, the present work links a canonical cerebellar synapse-organizing pathway defined in experimental models to a human hereditary ataxia.

In addition to motor features, all three affected individuals showed mild-to-moderate neurocognitive impairment (Table 1). Similar delays in speech and cognitive development have been reported in patients with *GRID2* variants,[17] raising the possibility that these findings reflect non-motor contributions of the cerebellum, including features related to cerebellar cognitive affective syndrome.[37] However, Cbln1 is also expressed outside the cerebellum, including in forebrain regions implicated in cognitive function.[38] Consistent with previous reports, we detected endogenous Cbln1 expression in the forebrain, including the hippocampus (Figure S7). Moreover, our previous study demonstrated that forebrain Cbln1 contributes to cognitive function,[38] raising

the possibility that *Cbln1*$^{Y112C/Y112C}$ mice may also exhibit cognitive deficits. Although cognitive behavior and forebrain synaptic function were not examined in the present study, future studies addressing these phenotypes may help clarify the contribution of extracerebellar CBLN1 dysfunction to the cognitive impairment observed in patients. Beyond synapse organization, Cbln1 has been implicated in axonal growth and guidance during development. [39] Some patients also showed extracerebellar abnormalities, including thinning of the corpus callosum, raising the possibility that impaired CBLN1 function perturbs long-range axonal development or maintenance in humans. Although our current data most strongly support synaptic deficiency as the proximate cause of cerebellar dysfunction, these findings motivate further work to define the developmental roles of CBLN1 across brain regions and to determine whether synaptic and axonal mechanisms contribute differentially to the broader clinical spectrum.

Patient-derived CBLN1 variants produce a functional extracellular null state

Our mechanistic data indicate that the pathogenic consequences of the CBLN1 variants identified here converge on marked loss of extracellular CBLN1 availability. The globular C1q domain is essential for oligomerization of C1q family proteins, and stable trimer formation is required for efficient forward trafficking through the secretory pathway.[40,41] Structural mapping places both A63 and Y112 near the trimer interface,[24] providing a plausible basis for impaired assembly and consequent alterations in protein stability, degradation, and/or trafficking. Consistent with this model, both patient-derived variants showed reduced steady-state intracellular abundance and defective maturation through early secretory compartments, together with near-complete loss of secretion. The reduced abundance of the mutant proteins could reflect decreased protein stability and/or enhanced degradation of improperly folded or assembled proteins, potentially through ER quality-control pathways, although these possibilities were not directly tested. Importantly, this trafficking defect translated directly into loss of synapse-organizing function: mutant CBLN1 failed to support GluD2-dependent presynaptic differentiation *in vitro*, and synaptic Cbln1 was

essentially absent in the knock-in cerebellum. These findings support a model in which mutant CBLN1 is synthesized but fails to reach the extracellular synaptic environment in amounts sufficient to sustain PF–PC synapse organization.

A useful parallel can be drawn with other C1q family proteins in which disease-associated substitutions destabilize the globular domain and cause intracellular retention. Mutations in collagen X (COL10A1), for example, impair trimer stability and secretion and cause Schmid metaphyseal chondrodysplasia.[42] Although the affected tissues and clinical manifestations differ, these disorders illustrate a shared principle: disruption of the C1q-domain interface can convert secreted proteins into secretion-defective alleles, leading to loss of extracellular function. In the cerebellum, this creates a functional extracellular null condition, explaining why the *Cbln1*^{Y112C} model phenocopies key features of Cbln1 deficiency despite continued intracellular production of mutant protein.

PF–PC synaptopathy drives defective CF refinement and impaired motor learning

The cerebellar phenotype of *Cbln1*$^{Y112C/Y112C}$ mice supports a hierarchical model in which loss of extracellular Cbln1 first compromises PF–PC synapse integrity and transmission, and secondarily disrupts postnatal CF refinement and mono-innervation. This interpretation is consistent with previous work showing that PF–PC synapses provide activity-dependent signals required to eliminate surplus CF inputs and restrict CF territory to proximal dendrites.[28,29] The increased size and vGluT1 signal intensity of the remaining presynaptic puncta, despite their reduced number, may represent structural remodeling or a compensatory response to impaired PF–PC connectivity. However, the accompanying increase in paired-pulse facilitation indicates that these changes do not reflect enhanced presynaptic release efficacy. Our data further show that synaptic dysfunction extends beyond structural disruption: PF–PC LTD was abolished, and animals displayed impaired cerebellar motor learning. Together, these findings define a mechanistic chain linking loss of an extracellular synaptic organizer to synapse architecture, circuit refinement, plasticity, and

behavior, and establish a framework for understanding how CBLN1 deficiency produces cerebellar dysfunction in humans.

An important implication is that a substantial component of the phenotype reflects circuit dysfunction that remains amenable to repair, rather than only fixed structural damage. Although the patients show cerebellar atrophy, the broad rescue observed in adult knock-in mice indicates that many circuit-level abnormalities remain reversible when extracellular CBLN1 is restored. Notably, AAV-mediated CBLN1 replacement also increased vermal cross-sectional and molecular layer areas and increased the estimated total Car8-positive dendritic length, indicating that structural abnormalities of the adult mutant cerebellum are at least partly reversible. These results strengthen the view that some inherited neurologic disorders can be understood, at least in part, as treatable synaptopathies, in which restoring missing synaptic components can meaningfully recover function even after symptom onset.

Astrocyte-targeted gene delivery enables durable extracellular CBLN1 replacement

A major advance of this study is the demonstration that long-term replacement of a secreted synaptic organizer can be achieved by using astrocytes as a cellular source of extracellular CBLN1. Previous studies showed that recombinant Cbln1 protein delivered directly to the cerebellum can rapidly ameliorate deficits in *Cbln1*-null mice,[10,31,43] indicating that core circuit abnormalities are not irrevocably fixed after development. Consistent with these previous findings, recombinant Cbln1 also improved rotarod performance in *Cbln1*$^{Y112C/Y112C}$ mice, but the effect was transient: significant improvement was observed on days 3–5, was no longer significant at the group level after day 8, and had returned to approximately pre-treatment levels by 3 weeks. Thus, protein delivery is limited by restricted distribution, short persistence, and the practical difficulty of repeated invasive administration. These constraints are likely to preclude durable rescue of phenotypes requiring sustained and widespread Cbln1 availability. Likewise, transient Sindbis virus-mediated expression of GluD2 in *Grid2*-null mice improves PF–PC synapse-related

phenotypes, but full normalization of downstream CF refinement and cerebellar learning has remained incomplete,[44] consistent with a requirement for broad and persistent reconstitution of the PF–PC organizing pathway. By contrast, systemic delivery of an astrocyte-targeted adeno-associated viral vector in adult *Cbln1*$^{Y112C/Y112C}$ mice restored synaptic CBLN1 localization and produced durable rescue across multiple levels, including pre- and postsynaptic alignment, PF transmission, CF mono-innervation, LTD, and behavior.

The choice of astrocytes as a source of CBLN1 was motivated by both conceptual and practical considerations. Because CBLN1 acts extracellularly, therapeutic efficacy is likely to depend primarily on extracellular availability and synaptic targeting rather than on expression in its endogenous neuronal source. Restricting transgene expression to non-neuronal cells may reduce the risk that ectopic neuronal expression alters synaptogenesis or circuit wiring. In addition, astrocytes are anatomically positioned to deliver secreted factors to synapses within the framework of the tripartite synapse,[45] and in the cerebellum Bergmann glial processes tightly ensheath PF–PC synapses,[33] providing an efficient microenvironment for local delivery of synaptic organizers. Astrocytes are also broadly distributed throughout the CNS, raising the possibility that the same strategy could be extended to extracerebellar regions relevant to cognitive phenotypes. Indeed, systemic PHP.eB delivery resulted in HA-CBLN1 expression in extracerebellar regions, including the hippocampus and cerebral cortex. Because this distribution differed from that of endogenous Cbln1, however, widespread expression could potentially produce both beneficial and unintended extracerebellar effects and will require careful evaluation in future studies. Consistent with this rationale, our control analyses did not reveal major changes in astrocyte-dependent glutamate clearance, supporting the interpretation that rescue primarily reflects restoration of extracellular CBLN1 rather than nonspecific enhancement of astrocytic homeostatic functions.

More broadly, our findings suggest that glial cells can be harnessed as durable sources of secreted therapeutic proteins for circuit repair in disorders caused by deficiency of extracellular

synapse-stabilizing factors. In this regard, astrocyte-targeted CBLN1 delivery may represent a broader therapeutic paradigm for diseases caused by loss of secreted synaptic organizers or other extracellular circuit-maintenance factors.

Limitations and future directions

This study has several limitations. First, the genetic evidence currently rests on two pedigrees and two missense variants. Although our functional studies and *in vivo* modeling strongly support causality, additional families and variants will be required to define the full clinical spectrum, penetrance, and genotype–phenotype correlations of *CBLN1*-related disease, including extracerebellar manifestations. Second, our mechanistic work has focused on the loss of extracellular CBLN1 availability; the extent to which reduced mutant protein stability, enhanced degradation, intracellular retention, ER stress, or other cell-autonomous effects contribute to the phenotype remains to be determined. Third, while the rescue experiments provide compelling proof of concept, translation will require further optimization of vector design, dosing, biodistribution, and safety, particularly with respect to systemic gene delivery, immune responses, the broader-than-endogenous distribution of transgene expression, and long-term control of transgene expression. Although improved spontaneous locomotion remained evident at 6 months, quantitative behavioral assessments were performed only at 1–2 months after treatment. Systematic longitudinal studies will therefore be required to define the durability of the therapeutic effect. It will also be important to determine the minimum level and spatial distribution of extracellular CBLN1 required for therapeutic benefit. Finally, the extent to which advanced disease with substantial cerebellar atrophy remains reversible is unknown. Defining therapeutic windows and identifying biomarkers of synaptic rescue will be important next steps toward clinical application.

MATERIALS AND METHODS

Human subjects and ethics

Affected individuals were evaluated by at least one pediatric neurologist (M.S.A., M.S.Z., or J.G.). Written informed consent was obtained from all participants or their legal guardians. Human studies were approved by the participating institutions and conducted in accordance with institutional and national ethical standards.

Animals

All recombinant DNA experiments were performed at Keio University in accordance with the guidelines of the Keio University School of Medicine Committee for Safety of Recombinant DNA Experiments (approval no. 16-087-2). All animal procedures were approved by the Animal Resource Committee of Keio University (protocol 09050-5) and were conducted in accordance with institutional guidelines.

Mice were housed under specific pathogen-free conditions on a 12-h light/12-h dark cycle with ad libitum access to food and water. Unless otherwise specified, experiments were performed using age-matched littermates analyzed within the same experimental series. Both sexes were used. Because no clear sex-dependent differences were detected in the cerebellar phenotypes examined, data from males and females were pooled unless otherwise indicated.

HA-Cbln1 knock-in mice were generated as described previously.[46]

Generation of *Cbln1*$^{Y112C/Y112C}$ knock-in mice

Cbln1$^{Y112C/Y112C}$ mice were generated in-house at Keio University by CRISPR/Cas9-mediated genome editing with minor modifications of a previously described method.[47] Zygotes were produced by *in vitro* fertilization using oocytes and sperm from B6D2F1 mice. SpCas9 protein (250 ng/mL; PNA Bio), Cbln1 crRNA (5 pmol/mL; 5′-AACTGTAGATGCCTTTGCGC-3′), tracrRNA (5 pmol/mL; Fasmac), and a 158-nt single-stranded oligodeoxynucleotide donor (ssODN; 500 ng/mL; Integrated DNA Technologies) carrying the Y112C substitution and

homology arms were assembled and incubated at 37°C for 15 min before electroporation. The donor also contained silent mutations that disrupted the PAM sequence (GGG to GGA) to prevent re-cutting and introduced a PstI site for genotyping.

Electroporation was performed using platinum block electrodes (GE-101, BEX) connected to a CUY21EDIT II electroporator (BEX) at 150 mA with six 3-ms pulses separated by 97-ms intervals. Zygotes were cultured at 37°C in 5% CO2 until the 2-cell stage and then transferred into the oviducts of pseudopregnant ICR females.

Genotyping and sequence confirmation

Genomic DNA was extracted from tail biopsies. The region flanking the crRNA target site was amplified by PCR using the following primers: forward, 5′-CATGAGCCGTCCGAGATGAG-3′; reverse, 5′-AGAAGGTGAGCGTGGAGGAG-3′. PCR products were sequenced directly or cloned into pMD20 (Takara Bio) before Sanger sequencing. Sequencing chromatograms were analyzed using CRISPR-ID.[48] Founder mice were backcrossed to C57BL/6N mice for at least three generations to minimize potential off-target effects.

Plasmids and AAV vectors

For heterologous expression and secretion assays, HA-tagged or FLAG-tagged human CBLN1 cDNA (WT, A63P, or Y112C) was cloned into pHLsec[49] under the control of the CAG promoter. pCAGGS-mCherry[50] was used as a negative control and/or transfection marker as indicated.

For AAV-mediated expression in cerebellar granule cells used in the artificial synapse formation assay, GFP in pAAV-Syn-GFP (Addgene #58867) was replaced with HA-tagged CBLN1-WT or 3×FLAG-tagged CBLN1-Y112C, followed by IRES-EGFP or IRES-TagRFP, respectively. For GluD2-ATD presentation in HEK293 cells, pCAGGS-Display-GluD2-ATD-myc was used.[24]

To test granule cell-targeted expression in vivo, the synapsin I promoter in pAAV-Syn-GFP

was replaced with a rat *Gabra6* minimal promoter (synthetic DNA; Eurofins Genomics) [32] inserted at the ApaI-BamHI sites, and GFP was replaced with HA-CBLN1-IRES-EGFP to generate pAAV-α6-HA-CBLN1-IRES-EGFP. For astrocyte-targeted expression, split-TurboID-CT in pZac2.1-gfaABC1D[34] was replaced with HA-CBLN1-IRES-EGFP to generate pZac2.1-gfaABC1D-HA-CBLN1-IRES-EGFP. A control vector lacking HA-CBLN1 (pZac2.1-gfaABC1D-IRES-EGFP) was used as a negative control.

For AAV packaging, pAAV-DJ and pHelper were obtained from Cell Biolabs. pUCmini-iCAP-PHP.eB (Addgene #103005) and pAdDeltaF6 (Addgene #112867) were obtained from Addgene.

All AAV vectors used in this study were single-stranded AAV (ssAAVs).

Antibodies

Primary and secondary antibodies, together with sources, catalog numbers, RRIDs, and working dilutions, are listed in Table S1. Nuclei were counterstained with DAPI (D1306, Invitrogen).

Recombinant AAV production, purification and titration

Recombinant AAVs were produced as previously described[34] using HEK293AAV cells (Cell Biolabs). For PHP.eB capsid production, cells were transfected with pAdDeltaF6, pUCmini-iCAP-PHP.eB, and the AAV vector plasmid using PEI Max (Polysciences, 24765-1). For AAV-DJ capsid production, cells were transfected with pHelper, pAAV-DJ, and the AAV vector plasmid using the calcium phosphate method.

Seventy-two hours after transfection, cells were harvested, lysed by repeated freeze-thaw cycles, and treated with benzonase (Millipore, 70664-3). Viral particles were purified by iodixanol gradient ultracentrifugation (OptiPrep; Abbott, AXS-1114542-250ML) and concentrated using Amicon Ultra 100-kDa filters (Millipore UFC910024). AAV-DJ preparations used for *in vitro* granule cell infection were purified using the AAVpro Purification Kit (Takara Bio, 6666) according to the manufacturer's instructions. Viral genome titers were determined by

574 quantitative PCR (QuantStudio 5, Thermo Fisher Scientific) using ITR primers (forward, 5′-
575 GGAACCCCTAGTGATGGAGTT-3′; reverse, 5′-CGGCCTCAGTGAGCGA-3′) and pAAV-
576 Syn-GFP (Addgene #58867) as the standard plasmid.
577
578 **Intracerebellar injection of AAV or recombinant Cbln1 protein**
579 Recombinant Cbln1 protein was prepared as described previously.[24] Briefly, HA-Cbln1-His was
580 expressed in Expi293 cells (A14645; ThermoFisher Scientific), and cells were cultured for 6 days.
581 The supernatant was collected and filtered, followed by dialysis against a buffer containing 20
582 mM Tris-HCl (pH 8.0), 500 mM NaCl, and 5 mM imidazole. The sample was purified by TALON
583 metal affinity resin (Clontech; 635520), and the protein was eluted with 20 mM Tris-HCl (pH
584 8.0), 500 mM NaCl, and 200 mM imidazole. The protein was dialyzed against 10 mM Hepes-
585 NaOH (pH 7.4) containing 150 mM NaCl. Final purification was performed by SEC using a
586 HiLoad Superdex 200 pg column (28989335; Cytiva) at 4 ˚C.
587 Direct cerebellar AAV injections were performed with minor modifications of previous
588 protocols. One-month-old mice were anesthetized by intraperitoneal injection of medetomidine
589 (0.3 mg/kg), midazolam (4.0 mg/kg), and butorphanol (5.0 mg/kg). AAV solution (5.0×10^{13}
590 vg/mL, 4 μL) or recombinant Cbln1 solution (3.27 μg/μL, 5 μL) was injected into the vermis of
591 lobules V–VIII using a glass micropipette (tip diameter, 30–40 μm) and a microinjector
592 (Nanoliter; World Precision Instruments) at 12 μL/h to a depth of 150–300 μm. The injection site
593 was positioned on the midline approximately 1 mm occipital to the junction between the
594 interparietal and occipital bones.
595 For recombinant Cbln1 treatment, 5 μL of purified Cbln1 solution (3.27 μg/μL) was delivered
596 into the subarachnoid space over the cerebellum as described previously.[7,10] Motor performance
597 was assessed longitudinally by rotarod testing before and after protein administration at the time
598 points indicated in Figure S5.
599

Systemic PHP.eB administration

For systemic delivery, PHP.eB-packaged AAV was administered to 1-month-old *Cbln1*$^{Y112C/Y112C}$ mice by retro-orbital injection as previously described[51] with minor modifications. Under the anesthetic regimen described above, the needle of a 30-gauge insulin syringe (BD 326638) was inserted into the retrobulbar space, and 50 μL of viral solution was delivered per session. Injections were performed on two consecutive days (total volume, 100 μL; 0.6–1.0 × 10^{13} vg/animal). Post-procedure analgesia and recovery monitoring were performed in accordance with institutional guidelines. Quantitative analyses were conducted 1–1.5 months after injection (Figure 6; Figures S6, S8, and S9; Movie S2). Spontaneous locomotor behavior was additionally recorded 6 months after injection (Movie S3).

Cell culture, secretion assays, and immunoblotting

HEK293 cells were maintained in DMEM supplemented with 10% fetal calf serum, 1 mM L-glutamine, and penicillin/streptomycin at 37°C in 5% CO_2. Cells were transfected using the calcium phosphate method. For secretion assays, the medium was replaced with CD293 medium supplemented with 1 mM L-glutamine, and conditioned medium was collected 3–4 days later.

Cells were lysed in buffer containing 0.5% Triton X-100, 20 mM Tris-HCl (pH 8.0), 150 mM NaCl, and 5 mM EDTA, sonicated, and adjusted to 1% SDS. Conditioned media and lysates were clarified by centrifugation (15,000 rpm, 5 min), separated by SDS-PAGE, and transferred to PVDF membranes. Immunoblotting was performed using HRP-conjugated secondary antibodies and chemiluminescent detection (Immobilon Western Chemiluminescent HRP substrate, Millipore WBKLS00500).

For assessment of AAV-driven expression *in vivo*, mice were euthanized 2 weeks after intracerebellar injection. Cerebella were dissected in cold PBS, snap-frozen in liquid nitrogen, homogenized in 20 mM Tris-HCl (pH 8.0), 150 mM NaCl, and 5 mM EDTA, adjusted to 1% SDS, sonicated, and quantified by BCA assay (Thermo Fisher Scientific) before SDS-PAGE.

626

627 **Deglycosylation assays**

628 HEK293 cells expressing HA-tagged CBLN1 (WT or mutant) were lysed in 20 mM Tris-HCl (pH
629 8.0), 150 mM NaCl, and 0.5% Triton X-100. Proteins were denatured at 100°C for 10 min in
630 0.5% SDS and 40 mM DTT, then incubated with PNGase F or Endo H (NEB) under the
631 manufacturer's recommended conditions. Deglycosylated proteins were analyzed by
632 immunoblotting with anti-HA antibody.

633

634 **Primary culture of cerebellar granule cells**

635 Primary cerebellar granule cells were prepared as previously described.[52] Briefly, P3–P5 WT or
636 *Cbln1* knockout mice were anesthetized on ice and decapitated. Cerebella were dissected,
637 enzymatically dissociated with trypsin, and plated on poly-L-lysine-coated glass coverslips at 1.5
638 × 10^3 cells/cm^2. Cells were maintained at 37°C in 5% CO_2. AAVs encoding WT CBLN1 or
639 Y112C (2.0 × 10^9 vg/mL) were applied at DIV0 immediately after plating and removed at DIV3
640 by replacing the medium with minimal essential medium containing insulin-transferrin-selenite
641 supplement (Sigma 11074547001), 2 mM glutamine, 5.0 g/L D-glucose, 0.02 mg/mL gentamicin,
642 and 4 μM AraC.

643

644 **Artificial synapse formation assay**

645 Artificial synapse formation assays were performed as previously described.[9] Briefly, HEK293
646 cells were transfected with myc-tagged GluD2-ATD pDisplay construct and added to cerebellar
647 granule cell cultures at DIV7, followed by 24 h of co-culture. Cells were fixed with 4%
648 paraformaldehyde in PBS, permeabilized with methanol at −20°C, and immunostained with anti-
649 vGluT1 and anti-myc antibodies. Images were acquired on an SD-OSR microscope (Olympus)
650 with a 60× objective.

651 HEK293 cells were identified by anti-myc labeling, and fields containing 1–3 cells were

selected. Z-stack images were acquired at 0.5-μm intervals (15–25 optical sections/cell), projected by maximum intensity, and subjected to background subtraction using a rolling-ball radius of 20 pixels. Regions of interest were defined from the myc signal using a constant threshold across all images. vGluT1 intensity within each region of interest was measured in ImageJ and normalized to the mean value for non-infected *Cbln1*-null granule cell cultures.

Immunohistochemistry and confocal imaging

Mice were deeply anesthetized and perfused transcardially with 4% paraformaldehyde in 0.1 M phosphate buffer (PB, pH 7.4). Brains were post-fixed and sectioned at 50 μm using a vibratome (DTK-1000, D.S.K.). For detection of synaptic Cbln1 and GluD2, sections were treated with pepsin (1 mg/mL; Dako) in 0.2 N HCl at 37°C for antigen retrieval. Sections were blocked in 5% normal donkey serum and incubated with primary antibodies followed by fluorescent secondary antibodies.

Images were acquired using confocal microscopy (FV1000 with 4×, 10×, 20× and 40× objectives and/or SD-OSR with a 100× objective; Olympus). For quantitative comparisons, sections from different genotypes or treatment groups were processed in parallel and imaged using identical acquisition settings. The cerebellar primary fissure was identified by DAPI staining, and regions of interest were placed in the molecular layer of lobules IV and V on either side of the fissure. Approximately nine non-overlapping images were acquired from a single section.

The cross-sectional area of the cerebellar vermis and the area of the molecular layer were quantified using ImageJ. ROIs encompassing the vermal cross section were defined by automatic thresholding, whereas molecular layer ROIs were manually delineated using the polygon selection tool.

To analyze Purkinje cell dendritic processes, confocal images of cerebellar sections stained for Car8 were processed in ImageJ by background subtraction using the rolling-ball method with a radius of 20 pixels, followed by thresholding using the Huang method and despeckling. An ROI

678 corresponding to the molecular layer was manually defined, and the image was skeletonized
679 within the ROI. The total length of skeletonized Car8-positive dendritic processes within each
680 ROI was measured and divided by the ROI area to obtain dendritic length density. For each mouse,
681 dendritic length density was averaged across the analyzed images and multiplied by the
682 corresponding molecular layer area to estimate the total Car8-positive dendritic length within the
683 vermal molecular layer. Statistical comparisons were performed using mouse-level values..

684 For analysis of vGluT1-positive puncta, puncta number, size, and fluorescence intensity were
685 quantified within molecular layer ROIs in ImageJ using identical segmentation criteria across
686 experimental groups.

687

688 **Electrophysiology**

689 Cerebellar slices were prepared from adult mice (P32–P63) as described previously.[53] Briefly,
690 mice were deeply anesthetized with isoflurane and decapitated. The brain was rapidly removed
691 and immediately immersed in ice-cold ACSF containing (in mM) 125 NaCl, 2.5 KCl, 2 $CaCl_2$, 1
692 $MgCl_2$, 1.25 NaH_2PO_4, 26 $NaHCO_3$, and 10 D-glucose, continuously bubbled with 95% O_2/5%
693 CO_2. The cerebellum was dissected from the brain, and parasagittal cerebellar slices (200 μm)
694 were prepared in ice-cold, oxygenated ACSF using a microslicer (LinearSlicer Pro7, D.S.K.).
695 After slicing, the slices were allowed to recover in oxygenated ACSF for at least 60 min at room
696 temperature before electrophysiology recordings. Picrotoxin (100 μM; Sigma-Aldrich) was
697 included to block inhibitory transmission.

698 Whole-cell recordings were obtained from visually identified Purkinje cells using a 60×
699 water-immersion objective on an upright microscope (BX51WI, Olympus) at room temperature.
700 Patch pipettes (1–3 MΩ) were filled with intracellular solution containing the following (in mM).
701 For CF-EPSC recordings: 150 Cs-gluconate, 10 HEPES, 4 $MgCl_2$, 4 Na_2ATP, 1 Na_2GTP, 0.4
702 EGTA, and 5 QX-314 (pH 7.25; 292 mOsm/kg). For PF-EPSC recordings and LTD
703 measurements: 65 Cs-methanesulfonate, 65 K-gluconate, 20 HEPES, 10 KCl, 1 $MgCl_2$, 4 Na_2ATP,

1 Na_2GTP, 5 sucrose, and 0.4 EGTA (pH 7.25; 295 mOsm/kg).

To evoke CF- and PF-EPSCs, Purkinje cells were voltage-clamped at −10 mV and −80 mV, respectively, and square pulses (10 μs, 0–200 μA) were delivered via a stimulating electrode placed in the granule cell layer or molecular layer (~50 μm below the pial surface), respectively. Selective stimulation was confirmed by paired-pulse depression for CFs and paired-pulse facilitation for PFs at a 50-ms interval. To reduce variability in CF maturation across lobules and microzones, recordings were restricted to Purkinje cells in the bank regions of lobules IV–VII.[54]

For LTD experiments, PF-EPSCs were recorded at 0.1 Hz from Purkinje cells voltage-clamped at −80 mV for at least 10 min to establish a stable baseline. LTD was induced by conjunctive stimulation consisting of 30 repetitions of a single PF stimulus paired with a 200-ms depolarizing step from −60 to +20 mV at 1 Hz.[44] Access resistance was monitored every 10 s using responses to 2-mV, 50-ms hyperpolarizing steps; recordings were excluded if access resistance changed by >20%. Signals were acquired using an Axopatch 200B amplifier and pClamp v9.2 (Molecular Devices), filtered at 1 kHz, and digitized at 4 kHz.

Behavioral analyses

Behavioral testing was performed during the light phase under identical experimental conditions across groups. Ages and post-injection time points are indicated in the figure legends. For experiments examining the duration of recombinant Cbln1-mediated rescue, rotarod performance was assessed longitudinally before and after protein administration at the time points indicated in Figure S5.

Motor coordination was assessed using a rotarod test with minor modifications of a previously described protocol.[10] Mice were placed on a 3-cm-diameter rod rotating at a constant 20 rpm for five trials, and the latency to fall (maximum, 60 s per trial) was averaged.

Gait was analyzed on a treadmill with minor modifications of a previously described method. [31] Mice walked on a treadmill belt at 16 m/min (O'hara & Co.), and locomotion was recorded at

120 frames/s using an iPad Pro (Apple). Videos were analyzed in ImageJ. Two-dimensional coordinates of the hindlimb toe were tracked manually, and maximal vertical displacement (toe height) was calculated. An average of 22–100 steps per mouse was used for analysis.

Spontaneous eye movements and horizontal optokinetic responses (hOKRs) were measured as previously described.[17,53] For head fixation, mice were anesthetized with medetomidine/midazolam/butorphanol (0.75/4/5 mg/kg, i.p.), and a flat-head screw was affixed to the skull with dental resin (Super-Bond, Sun Medical). Anesthesia was reversed with atipamezole (5 mg/kg, i.p.). After at least 3 days of recovery, mice were habituated to the head-fixed condition before data acquisition. Mice were head-fixed with the body loosely restrained in a plastic cylinder under room illumination (300–400 lux), and eye movements were recorded using an infrared camera.

For spontaneous eye movement recordings, 15-s traces were collected five times during the resting state. hOKRs were elicited by horizontal sinusoidal oscillation of a checkerboard pattern (check size, 2 cm; screen height, 55 cm; oscillation, 15° peak-to-peak at 0.33 Hz). For adaptation, the stimulus was presented continuously for 1 h. Eye traces free of blinks and saccades (≥10 cycles) were averaged, and amplitudes were extracted by modified Fourier analysis.[53] Gain was defined as the ratio of peak-to-peak eye movement amplitude to peak-to-peak stimulus amplitude.

Study design and statistical analysis

For *in vivo* histology, electrophysiology, and behavioral experiments, comparisons were made between the indicated genotypes and/or treatment groups analyzed in parallel. For rescue experiments, mice injected with CBLN1-expressing AAV vectors were compared with mice injected with the corresponding control vectors. For secretion and deglycosylation assays, the experimental unit was an independent transfection sample. For artificial synapse formation assays, the experimental unit was an individually quantified myc-positive HEK293 cell obtained from independently prepared co-cultures, as detailed in the figure legends. For *in vivo* histologic and

behavioral assays, the experimental unit was a single section. For electrophysiology, the experimental unit was a single recorded Purkinje cell, with cells sampled from multiple mice; the numbers of cells and mice are reported in the figure legends.

Electrophysiological, behavioral, and eye-movement datasets were analyzed blinded to genotype and treatment. Data are presented as mean ± SEM unless otherwise stated. Exact values of n and the statistical tests used are reported in the figure legends. Individual data points are shown where appropriate.

Statistical analyses were performed using GraphPad Prism 9 (GraphPad Software) and/or BellCurve for Excel (Social Survey Research Information Co.). For comparisons between two groups, two-tailed Mann-Whitney U tests were used when data did not meet assumptions for parametric testing or when normality could not be assumed. For comparisons among multiple groups, Kruskal-Wallis tests followed by the post hoc multiple-comparison tests specified in the corresponding figure legends. For analyses involving two factors, including group and time, two-way ANOVA followed by Bonferroni post hoc tests was used as indicated. Distributional assumptions were evaluated in GraphPad Prism together with visual inspection of data distribution. When assumptions for parametric analysis were not met, nonparametric tests were used instead. Statistical significance was defined as $P < 0.05$.

DATA AVAILABILITY STATEMENT

Knock-in mouse lines used in this study will be distributed on request. All data generated or analyzed during this study are included in this article and its supplemental information files. Values for all data points in graphs are reported in the Supporting Data Values file.

ACKNOWLEDGEMENTS

We thank Dr. Scott Soderling (Duke University School of Medicine, USA) for providing an astrocyte-expressing AAV vector (pZac2.1-gfaABC1D-split-turboID-CT). This work was

supported by the Grant-in-Aid for Science Research from the Ministry of Education, Culture, Sports, Science and Technology of Japan (24K09661 to T.Y., 24K02212, and 22K19364 to W.K. and 22K21353, 25H01011 to M.Y.), the Takeda Science Foundation (T.Y. and W.K.), the Kanae Foundation (T.Y.), the Inamori Research Foundation (T.Y.), and the Kowa Life Science Foundation (T.Y.), the Naito Foundation (W.K.), the Brain Science Foundation (W.K.), AMED (Grant Numbers JP24zf0127010 to M.Y) and the Science and Technology Development Fund (STDF), Egypt (Grant number: 33650) to M.S.Z, M.S.A.

AUTHOR CONTRIBUTIONS

Conceptualization, methodology, and writing - original draft preparation, T.Y.; methodology, funding acquisition and writing - original draft preparation, W.K.; resources, A.H.; resources, N.O.; resources, T.T.; resources, K.M.; resources, K.T.; clinical investigation, M.S.A.; clinical investigation, M.S.Z.; clinical investigation, J.G.; conceptualization, funding acquisition, supervision, and writing – review & editing, M.Y.

DECLARATION OF INTERESTS

The authors declare no competing financial interests.

KEYWORDS:

cerebellar ataxia; synaptopathy; CBLN1; secretion defect; gene therapy; optokinetic response

802 **REFERENCES**

803 1. Klockgether, T., Mariotti, C., and Paulson, H.L. (2019). Spinocerebellar ataxia. Nat Rev Dis
804 Primers *5*, 24. https://doi.org/10.1038/s41572-019-0074-3.

805 2. Sailer, A., and Houlden, H. (2012). Recent Advances in the Genetics of Cerebellar Ataxias. Curr
806 Neurol Neurosci Rep *12*, 227–236. https://doi.org/10.1007/s11910-012-0267-6.

807 3. Beaudin, M., Matilla-Dueñas, A., Soong, B.-W., Pedroso, J.L., Barsottini, O.G., Mitoma, H.,
808 Tsuji, S., Schmahmann, J.D., Manto, M., Rouleau, G.A., et al. (2019). The Classification of
809 Autosomal Recessive Cerebellar Ataxias: a Consensus Statement from the Society for Research
810 on the Cerebellum and Ataxias Task Force. Cerebellum *18*, 1098–1125.
811 https://doi.org/10.1007/s12311-019-01052-2.

812 4. Grant, S.G. (2012). Synaptopathies: diseases of the synaptome. Current Opinion in Neurobiology
813 *22*, 522–529. https://doi.org/10.1016/j.conb.2012.02.002.

814 5. Yuzaki, M. (2011). Cbln1 and its family proteins in synapse formation and maintenance. Current
815 Opinion in Neurobiology *21*, 215–220. https://doi.org/10.1016/j.conb.2011.01.010.

816 6. Ibata, K., Kono, M., Narumi, S., Motohashi, J., Kakegawa, W., Kohda, K., and Yuzaki, M. (2019).
817 Activity-Dependent Secretion of Synaptic Organizer Cbln1 from Lysosomes in Granule Cell
818 Axons. Neuron *102*, 1184-1198.e10. https://doi.org/10.1016/j.neuron.2019.03.044.

819 7. Matsuda, K., Miura, E., Miyazaki, T., Kakegawa, W., Emi, K., Narumi, S., Fukazawa, Y., Ito-
820 Ishida, A., Kondo, T., Shigemoto, R., et al. (2010). Cbln1 Is a Ligand for an Orphan Glutamate
821 Receptor δ2, a Bidirectional Synapse Organizer. Science *328*, 363–368.
822 https://doi.org/10.1126/science.1185152.

823 8. Uemura, T., Lee, S.-J., Yasumura, M., Takeuchi, T., Yoshida, T., Ra, M., Taguchi, R., Sakimura,
824 K., and Mishina, M. (2010). *Trans*-Synaptic Interaction of GluRδ2 and Neurexin through Cbln1
825 Mediates Synapse Formation in the Cerebellum. Cell *141*, 1068–1079.
826 https://doi.org/10.1016/j.cell.2010.04.035.

827 9. Matsuda, K., and Yuzaki, M. (2011). Cbln family proteins promote synapse formation by
828 regulating distinct neurexin signaling pathways in various brain regions. European Journal of
829 Neuroscience *33*, 1447–1461. https://doi.org/10.1111/j.1460-9568.2011.07638.x.

830 10. Ito-Ishida, A., Miura, E., Emi, K., Matsuda, K., Iijima, T., Kondo, T., Kohda, K., Watanabe, M.,
831 and Yuzaki, M. (2008). Cbln1 Regulates Rapid Formation and Maintenance of Excitatory
832 Synapses in Mature Cerebellar Purkinje Cells In Vitro and In Vivo. J. Neurosci. *28*, 5920–5930.
833 https://doi.org/10.1523/JNEUROSCI.1030-08.2008.

834 11. Ito-Ishida, A., Miyazaki, T., Miura, E., Matsuda, K., Watanabe, M., Yuzaki, M., and Okabe, S.
835 (2012). Presynaptically Released Cbln1 Induces Dynamic Axonal Structural Changes by
836 Interacting with GluD2 during Cerebellar Synapse Formation. Neuron *76*, 549–564.
837 https://doi.org/10.1016/j.neuron.2012.07.027.

838 12. Hirai, H., Pang, Z., Bao, D., Miyazaki, T., Li, L., Miura, E., Parris, J., Rong, Y., Watanabe, M.,
839 Yuzaki, M., et al. (2005). Cbln1 is essential for synaptic integrity and plasticity in the cerebellum.
840 Nat Neurosci *8*, 1534–1541. https://doi.org/10.1038/nn1576.

841 13. Ito, M. (2001). Cerebellar Long-Term Depression: Characterization, Signal Transduction, and
842 Functional Roles. Physiological Reviews *81*, 1143–1195.

https://doi.org/10.1152/physrev.2001.81.3.1143.

14. Lek, M., Karczewski, K.J., Minikel, E.V., Samocha, K.E., Banks, E., Fennell, T., O'Donnell-Luria, A.H., Ware, J.S., Hill, A.J., Cummings, B.B., et al. (2016). Analysis of protein-coding genetic variation in 60,706 humans. Nature *536*, 285–291. https://doi.org/10.1038/nature19057.

15. Karczewski, K.J., Francioli, L.C., Tiao, G., Cummings, B.B., Alföldi, J., Wang, Q., Collins, R.L., Laricchia, K.M., Ganna, A., Birnbaum, D.P., et al. (2020). The mutational constraint spectrum quantified from variation in 141,456 humans. Nature *581*, 434–443. https://doi.org/10.1038/s41586-020-2308-7.

16. Allen, J.P., Garber, K.B., Perszyk, R., Khayat, C.T., Kell, S.A., Kaneko, M., Quindipan, C., Saitta, S., Ladda, R.L., Hewson, S., et al. (2024). Clinical features, functional consequences, and rescue pharmacology of missense GRID1 and GRID2 human variants. Hum Mol Genet *33*, 355–373. https://doi.org/10.1093/hmg/ddad188.

17. Hills, L.B., Masri, A., Konno, K., Kakegawa, W., Lam, A.-T.N., Lim-Melia, E., Chandy, N., Hill, R.S., Partlow, J.N., Al-Saffar, M., et al. (2013). Deletions in GRID2 lead to a recessive syndrome of cerebellar ataxia and tonic upgaze in humans. Neurology *81*, 1378–1386. https://doi.org/10.1212/WNL.0b013e3182a841a3.

18. Utine, G.E., Haliloğlu, G., Salancı, B., Çetinkaya, A., Kiper, P.Ö., Alanay, Y., Aktaş, D., Boduroğlu, K., and Alikaşifoğlu, M. (2013). A Homozygous Deletion in GRID2 Causes a Human Phenotype With Cerebellar Ataxia and Atrophy. J Child Neurol *28*, 926–932. https://doi.org/10.1177/0883073813484967.

19. Van Schil, K., Meire, F., Karlstetter, M., Bauwens, M., Verdin, H., Coppieters, F., Scheiffert, E., Van Nechel, C., Langmann, T., Deconinck, N., et al. (2015). Early-onset autosomal recessive cerebellar ataxia associated with retinal dystrophy: new human hotfoot phenotype caused by homozygous *GRID2* deletion. Genetics in Medicine *17*, 291–299. https://doi.org/10.1038/gim.2014.95.

20. Maier, A., Klopocki, E., Horn, D., Tzschach, A., Holm, T., Meyer, R., and Meyer, T. (2014). De novo partial deletion in GRID2 presenting with complicated spastic paraplegia. Muscle & Nerve *49*, 289–292. https://doi.org/10.1002/mus.24096.

21. Kashiwabuchi, N., Ikeda, K., Araki, K., Hirano, T., Shibuki, K., Takayama, C., Inoue, Y., Kutsuwada, T., Yagi, T., Kang, Y., et al. (1995). Impairment of motor coordination, Purkinje cell synapse formation, and cerebellar long-term depression in GluRδ2 mutant mice. Cell *81*, 245–252. https://doi.org/10.1016/0092-8674(95)90334-8.

22. Yoshida, T., Katoh, A., Ohtsuki, G., Mishina, M., and Hirano, T. (2004). Oscillating Purkinje Neuron Activity Causing Involuntary Eye Movement in a Mutant Mouse Deficient in the Glutamate Receptor δ2 Subunit. J. Neurosci. *24*, 2440–2448. https://doi.org/10.1523/JNEUROSCI.0783-03.2004.

23. Bao, D., Pang, Z., and Morgan, J.I. (2005). The structure and proteolytic processing of Cbln1 complexes. Journal of Neurochemistry *95*, 618–629. https://doi.org/10.1111/j.1471-4159.2005.03385.x.

24. Elegheert, J., Kakegawa, W., Clay, J.E., Shanks, N.F., Behiels, E., Matsuda, K., Kohda, K., Miura, E., Rossmann, M., Mitakidis, N., et al. (2016). Structural basis for integration of GluD receptors within synaptic organizer complexes. Science *353*, 295–299. https://doi.org/10.1126/science.aae0104.

25. Chun, D.K., McEwen, J.M., Burbea, M., and Kaplan, J.M. (2008). UNC-108/Rab2 Regulates Postendocytic Trafficking in Caenorhabditis elegans. MBoC *19*, 2682–2695. https://doi.org/10.1091/mbc.e07-11-1120.

26. Miura, E., Matsuda, K., Morgan, J.I., Yuzaki, M., and Watanabe, M. (2009). Cbln1 accumulates and colocalizes with Cbln3 and GluRδ2 at parallel fiber–Purkinje cell synapses in the mouse cerebellum. European Journal of Neuroscience *29*, 693–706. https://doi.org/10.1111/j.1460-9568.2009.06632.x.

27. Kakegawa, W., Paternain, A.V., Matsuda, K., Aller, M.I., Iida, I., Miura, E., Nozawa, K., Yamasaki, T., Sakimura, K., Yuzaki, M., et al. (2024). Kainate receptors regulate synaptic integrity and plasticity by forming a complex with synaptic organizers in the cerebellum. Cell Rep *43*, 114427. https://doi.org/10.1016/j.celrep.2024.114427.

28. Hashimoto, K., Yoshida, T., Sakimura, K., Mishina, M., Watanabe, M., and Kano, M. (2009). Influence of parallel fiber–Purkinje cell synapse formation on postnatal development of climbing fiber–Purkinje cell synapses in the cerebellum. Neuroscience *162*, 601–611. https://doi.org/10.1016/j.neuroscience.2008.12.037.

29. Kano, M., Watanabe, T., Uesaka, N., and Watanabe, M. (2018). Multiple Phases of Climbing Fiber Synapse Elimination in the Developing Cerebellum. Cerebellum *17*, 722–734. https://doi.org/10.1007/s12311-018-0964-z.

30. Cesa, R., and Strata, P. (2009). Axonal competition in the synaptic wiring of the cerebellar cortex during development and in the mature cerebellum. Neuroscience *162*, 624–632. https://doi.org/10.1016/j.neuroscience.2009.02.061.

31. Takeuchi, E., Ito-Ishida, A., Yuzaki, M., and Yanagihara, D. (2018). Improvement of cerebellar ataxic gait by injecting Cbln1 into the cerebellum of cbln1-null mice. Sci Rep *8*, 6184. https://doi.org/10.1038/s41598-018-24490-0.

32. Kim, Y., Kim, T., Rhee, J.K., Lee, D., Tanaka-Yamamoto, K., and Yamamoto, Y. (2015). Selective transgene expression in cerebellar Purkinje cells and granule cells using adeno-associated viruses together with specific promoters. Brain Res *1620*, 1–16. https://doi.org/10.1016/j.brainres.2015.05.015.

33. Iino, M., Goto, K., Kakegawa, W., Okado, H., Sudo, M., Ishiuchi, S., Miwa, A., Takayasu, Y., Saito, I., Tsuzuki, K., et al. (2001). Glia-Synapse Interaction Through Ca2+-Permeable AMPA Receptors in Bergmann Glia. Science *292*, 926–929. https://doi.org/10.1126/science.1058827.

34. Takano, T., Wallace, J.T., Baldwin, K.T., Purkey, A.M., Uezu, A., Courtland, J.L., Soderblom, E.J., Shimogori, T., Maness, P.F., Eroglu, C., et al. (2020). Chemico-genetic discovery of astrocytic control of inhibition in vivo. Nature *588*, 296–302. https://doi.org/10.1038/s41586-020-2926-0.

35. Shimamoto, K., Sakai, R., Takaoka, K., Yumoto, N., Nakajima, T., Amara, S.G., and Shigeri, Y. (2004). Characterization of Novel L-*threo*-β-Benzyloxyaspartate Derivatives, Potent Blockers of the Glutamate Transporters. Molecular Pharmacology *65*, 1008–1015. https://doi.org/10.1124/mol.65.4.1008.

36. Landrum, M.J., Lee, J.M., Benson, M., Brown, G.R., Chao, C., Chitipiralla, S., Gu, B., Hart, J., Hoffman, D., Jang, W., et al. (2018). ClinVar: improving access to variant interpretations and supporting evidence. Nucleic Acids Res *46*, D1062–D1067. https://doi.org/10.1093/nar/gkx1153.

37. Schmahmann, J.D. (2004). Disorders of the Cerebellum: Ataxia, Dysmetria of Thought, and the Cerebellar Cognitive Affective Syndrome. JNP *16*, 367–378. https://doi.org/10.1176/jnp.16.3.367.

38. Otsuka, S., Konno, K., Abe, M., Motohashi, J., Kohda, K., Sakimura, K., Watanabe, M., and Yuzaki, M. (2016). Roles of Cbln1 in Non-Motor Functions of Mice. J. Neurosci. *36*, 11801–11816. https://doi.org/10.1523/JNEUROSCI.0322-16.2016.

39. Han, P., She, Y., Yang, Z., Zhuang, M., Wang, Q., Luo, X., Yin, C., Zhu, J., Jaffrey, S.R., and Ji, S.-J. (2022). Cbln1 regulates axon growth and guidance in multiple neural regions. PLOS Biology *20*, e3001853. https://doi.org/10.1371/journal.pbio.3001853.

40. Iijima, T., Miura, E., Matsuda, K., Kamekawa, Y., Watanabe, M., and Yuzaki, M. (2007). Characterization of a transneuronal cytokine family Cbln − regulation of secretion by heteromeric assembly. European Journal of Neuroscience *25*, 1049–1057. https://doi.org/10.1111/j.1460-9568.2007.05361.x.

41. Bao, D., Pang, Z., Morgan, M.A., Parris, J., Rong, Y., Li, L., and Morgan, J.I. (2006). Cbln1 Is Essential for Interaction-Dependent Secretion of Cbln3. Molecular and Cellular Biology *26*, 9327–9337. https://doi.org/10.1128/MCB.01161-06.

42. Bogin, O., Kvansakul, M., Rom, E., Singer, J., Yayon, A., and Hohenester, E. (2002). Insight into Schmid Metaphyseal Chondrodysplasia from the Crystal Structure of the Collagen X NC1 Domain Trimer. Structure *10*, 165–173. https://doi.org/10.1016/S0969-2126(02)00697-4.

43. Emi, K., Kakegawa, W., Miura, E., Ito-Ishida, A., Kohda, K., and Yuzaki, M. (2013). Reevaluation of the role of parallel fiber synapses in delay eyeblink conditioning in mice using Cbln1 as a tool. Front Neural Circuits *7*, 180. https://doi.org/10.3389/fncir.2013.00180.

44. Kakegawa, W., Miyazaki, T., Kohda, K., Matsuda, K., Emi, K., Motohashi, J., Watanabe, M., and Yuzaki, M. (2009). The N-Terminal Domain of GluD2 (GluRδ2) Recruits Presynaptic Terminals and Regulates Synaptogenesis in the Cerebellum In Vivo. J. Neurosci. *29*, 5738–5748. https://doi.org/10.1523/JNEUROSCI.6013-08.2009.

45. Araque, A., Parpura, V., Sanzgiri, R.P., and Haydon, P.G. (1999). Tripartite synapses: glia, the unacknowledged partner. Trends in Neurosciences *22*, 208–215. https://doi.org/10.1016/S0166-2236(98)01349-6.

46. Nozawa, K., Sogabe, T., Hayashi, A., Motohashi, J., Miura, E., Arai, I., and Yuzaki, M. (2022). In vivo nanoscopic landscape of neurexin ligands underlying anterograde synapse specification. Neuron *110*, 3168-3185.e8. https://doi.org/10.1016/j.neuron.2022.07.027.

47. Nozawa, K., Hayashi, A., Motohashi, J., Takeo, Y.H., Matsuda, K., and Yuzaki, M. (2018). Cellular and Subcellular Localization of Endogenous Neuroligin-1 in the Cerebellum. Cerebellum *17*, 709–721. https://doi.org/10.1007/s12311-018-0966-x.

48. Dehairs, J., Talebi, A., Cherifi, Y., and Swinnen, J.V. (2016). CRISP-ID: decoding CRISPR mediated indels by Sanger sequencing. Sci Rep *6*, 28973. https://doi.org/10.1038/srep28973.

49. Aricescu, A.R., Lu, W., and Jones, E.Y. (2006). A time- and cost-efficient system for high-level protein production in mammalian cells. Acta Cryst D *62*, 1243–1250. https://doi.org/10.1107/S0907444906029799.

50. Nishiyama, J., Hayashi, Y., Nomura, T., Miura, E., Kakegawa, W., and Yuzaki, M. (2012).

969 Selective and regulated gene expression in murine Purkinje cells by in utero electroporation.
970 European Journal of Neuroscience *36*, 2867–2876. https://doi.org/10.1111/j.1460-
971 9568.2012.08203.x.

972 51. Yardeni, T., Eckhaus, M., Morris, H.D., Huizing, M., and Hoogstraten-Miller, S. (2011). Retro-
973 orbital injections in mice. Lab Anim *40*, 155–160. https://doi.org/10.1038/laban0511-155.

974 52. Martenson, J.S., Yamasaki, T., Chaudhury, N.H., Albrecht, D., and Tomita, S. (2017). Assembly
975 rules for GABAA receptor complexes in the brain. eLife *6*, e27443.
976 https://doi.org/10.7554/eLife.27443.

977 53. Kakegawa, W., Mitakidis, N., Miura, E., Abe, M., Matsuda, K., Takeo, Y.H., Kohda, K.,
978 Motohashi, J., Takahashi, A., Nagao, S., et al. (2015). Anterograde C1ql1 Signaling Is Required
979 in Order to Determine and Maintain a Single-Winner Climbing Fiber in the Mouse Cerebellum.
980 Neuron *85*, 316–329. https://doi.org/10.1016/j.neuron.2014.12.020.

981 54. Nishiyama, H., and Linden, D.J. (2004). Differential Maturation of Climbing Fiber Innervation
982 in Cerebellar Vermis. J. Neurosci. *24*, 3926–3932. https://doi.org/10.1523/JNEUROSCI.5610-
983 03.2004.

Figure Legends

Figure 1. Biallelic *CBLN1* variants are associated with an early-onset cerebellar syndrome with oculomotor abnormalities and cerebellar atrophy.

(A) Pedigrees of families 1613 and 24661. Double horizontal lines indicate consanguinity. Filled symbols denote affected individuals.

(B) Representative midsagittal T1-weighted MRI images obtained at the indicated ages, showing cerebellar atrophy with prominent vermian volume loss. Personally identifiable information on the original MRI films was masked during image processing.

(C) Summary of the biallelic *CBLN1* missense variants identified in affected individuals, including genomic and predicted protein annotations.

(D, E) Representative Sanger sequencing chromatograms for (**D**) the *CBLN1* c.335A>G variant in family 1613 and (**E**) the *CBLN1* c.187G>C variant in family 24661. Arrows indicate the variant nucleotide positions. Heterozygous carrier traces show overlapping A/G peaks (**D**) or G/C peaks (**E**), whereas affected individuals show a single peak consistent with homozygosity.

Figure 2. Patient-derived *CBLN1* variants show reduced protein abundance, impaired forward trafficking and secretion, and fail to support GluD2-dependent excitatory synapse formation *in vitro*.

(A) Domain organization of CBLN1. SS, signal sequence; CRR, cysteine-rich region; gC1q, globular C1q domain. The positions of the A63P and Y112C variants are indicated.

(B) Structure of the CBLN1 gC1q domain (PDB: 5KC5), shown as a monomer (left) and trimer (right). Variant residues are highlighted.

(C) Immunoblot analysis of HA-tagged CBLN1-WT, CBLN1-A63P, or CBLN1-Y112C expressed in HEK293 cells. Conditioned media and corresponding cell lysates were immunoblotted with anti-HA antibody; GAPDH served as a loading control for cell lysates. 1×, 3×, and 10× indicate increasing amounts of transfected cDNA. Both mutant proteins showed

reduced intracellular abundance and were not detectably secreted into the conditioned medium under these conditions. Representative of 3 independent experiments.

(D) Endoglycosidase sensitivity assay. Cell lysates expressing HA-tagged CBLN1 constructs were treated with Endo H or PNGase F and immunoblotted with anti-HA antibody to assess glycan maturation. The Endo H-resistant fraction was markedly reduced for CBLN1-A63P and CBLN1-Y112C, consistent with impaired forward trafficking through the secretory pathway. Representative of 4 independent experiments.

(E) Artificial synapse-formation assay. Wild-type or *Cbln1*-knockout (KO) cerebellar granule cells were co-cultured with HEK293 cells expressing the amino-terminal domain (ATD) of GluD2. Presynaptic differentiation was quantified as vGluT1 accumulation on GluD2-ATD-expressing HEK293 cells. AAV-mediated expression of CBLN1-WT, but not CBLN1-Y112C, restored synapse-inducing activity in *Cbln1*-KO granule cells. Scale bar, 10 μm. Data are mean ± SEM; dots indicate individual myc-positive HEK293 cells. n = 9 cells (WT), 10 cells (*Cbln1* KO), 9 cells (*Cbln1 KO* + CBLN1-WT), and 10 cells (*Cbln1* KO + CBLN1-Y112C) from 2 independent experiments. *$P < 0.05$, ***$P < 0.001$, Kruskal–Wallis test followed by Dunn's multiple-comparisons test.

Figure 3. *Cbln1*$^{Y112C/Y112C}$ knock-in mice lack synaptic Cbln1 and exhibit cerebellar motor and oculomotor abnormalities.

(A) CRISPR–Cas9 strategy used to generate the *Cbln1*$^{Y112C/Y112C}$ knock-in allele. The crRNA target sequence is indicated.

(B) Representative cerebellar sections from wild-type and *Cbln1*$^{Y112C/Y112C}$ mice immunostained for Car8, a PC marker, with DAPI counterstaining. Scale bar, 500 μm. Quantification (right) shows molecular layer thickness, vermal cross-sectional area, and molecular layer area. Molecular layer thickness was measured from the pial surface to the PC layer at the primary fissure. n = 8 sections from 4 mice per genotype. Vermal cross-sectional area and molecular layer area were

quantified in cross-sections of the cerebellar vermis. $n = 8$ sections from 4 mice per genotype.

(C) Representative confocal images of pepsin-treated cerebellar sections stained for Cbln1 and GluD2 to visualize synaptic puncta in the molecular layer. Scale bar, 4 μm.

(D) Rotarod performance at 20 rpm, shown as the mean latency to fall across five trials. $n = 7$ wild-type mice and 8 *Cbln1*$^{Y112C/Y112C}$ mice.

(E) Treadmill gait analysis at 16 m/min. Maximal hindlimb toe height was quantified. $n = 4$ wild-type mice and 5 *Cbln1*$^{Y112C/Y112C}$ mice.

(F) Spontaneous eye movements. Total eye movement distance during 15 s was quantified. $n = 7$ wild-type mice and 6 *Cbln1*$^{Y112C/Y112C}$ mice.

Data are mean ± SEM; dots indicate individual sections (**B**) or mice (**D–F**). *$P < 0.05$, **$P < 0.01$, ***$P < 0.001$, Mann–Whitney U test.

Figure 4. Cbln1-Y112C disrupts PF–PC synapse organization and impairs CF refinement.

(A, B) PF–PC synaptic marker distribution.

(A) Representative confocal images of pepsin-treated molecular layer stained for vGluT1, a PF presynaptic marker, and GluD2, a postsynaptic marker. Scale bar, 4 μm.

(B) Pixel intensity scatter plots and Pearson's correlation coefficients quantifying the relationship between vGluT1 and GluD2 signals. $n = 8$ sections from 4 mice per genotype.

(C, D) PF-evoked EPSCs. A schematic shows the stimulation and recording configuration.

(C) Input–output relationship of PF-evoked EPSCs.

(D) Paired-pulse ratio of PF-EPSC amplitudes (second/first) at a 50-ms interstimulus interval . $n = 16$ cells from 5 wild-type mice and 17 cells from 5 *Cbln1*$^{Y112C/Y112C}$ mice.

(E) CF territory in the molecular layer. Representative sections stained for vGluT2, a CF terminal marker, and Car8. Dotted lines indicate the pial surface, and asterisks indicate Purkinje cell somata. Scale bar, 20 μm. Quantification (right) shows normalized CF terminal height within the molecular layer. $n = 8$ sections from 4 mice per genotype.

(F–H) Functional CF innervation.

(F) Representative CF-EPSC traces recorded at increasing stimulus intensities.

(G) Distribution of the number of CF inputs per Purkinje cell. n = 30 cells from 6 mice for each genotype.

(H) Amplitude of the strongest CF-EPSC. n = 30 cells from 6 mice for each genotype.

Data are mean ± SEM. *P < 0.05, ***P < 0.001, Mann–Whitney U test (**B, D, E, G, H**) or two-way ANOVA followed by Bonferroni multiple-comparisons test (**C**).

Figure 5. Cbln1-Y112C abolishes PF–PC LTD and cerebellar motor learning.

(A) Schematic of LTD induction at PF–PC synapses using conjunctive stimulation (LTD-stim; 30 pairings of PF stimulation with Purkinje cell depolarization at 1 Hz).

(B, C) PF–PC LTD in wild-type and *Cbln1*$^{Y112C/Y112C}$ mice.

(B) Time course of PF-EPSC amplitudes normalized to baseline. Representative traces recorded at the indicated time points are shown above.

(C) Cumulative distribution of LTD magnitude 30 min after induction. n = 8 cells from 5 wild-type mice and 7 cells from 5 *Cbln1*$^{Y112C/Y112C}$ mice.

(D) Schematic of hOKR recording during sinusoidal oscillation of a checkerboard screen (15°). Representative hOKR traces before training (0 min) and after 60 min of training are shown for wild-type and *Cbln1*$^{Y112C/Y112C}$ mice.

(E) Individual (left) and mean (right) time courses of hOKR gain during training. n = 5 wild-type mice and 6 *Cbln1*$^{Y112C/Y112C}$ mice.

Data are mean ± SEM. *P < 0.05, ***P < 0.001, Mann–Whitney U test (**B, C**) or two-way ANOVA followed by Bonferroni multiple-comparisons test (**E**).

Figure 6. Systemic astrocyte-targeted AAV-mediated CBLN1 delivery restores synaptic function and reverses cerebellar synaptopathy in adult *Cbln1*$^{Y112C/Y112C}$ mice.

(A) Experimental design. AAV vectors expressing HA-CBLN1 or control construct (mock) under the astrocyte-specific *GfaABC1D* promoter were delivered by retro-orbital injection to 1-month-old *Cbln1*$^{Y112C/Y112C}$ mice. Analyses were performed 1–1.5 months later.

(B) Restoration of synaptic CBLN1 localization. Representative confocal images of pepsin-treated molecular layer stained for Cbln1 and GluD2. Wild-type cerebellum processed in parallel is shown for reference. Scale bar, 4 μm.

(C) PF–PC synapse organization after rescue. Representative molecular layer images stained for vGluT1 and GluD2, with corresponding pixel intensity scatter plots and Pearson's correlation coefficients. Scale bar, 4 μm

(D) PF–PC synaptic transmission after rescue. Input-output relationships and paired-pulse ratios of PF-EPSCs in mock-treated and HA-CBLN1-treated mutant mice. n = 16 cells from 5 mock-treated mutant mice and 17 cells from 5 HA-CBLN1-treated mutant mice.

(E, F) CF refinement after rescue.

(E) Distribution of the number of CF inputs per Purkinje cell after rescue.

(F) Amplitude of the strongest CF-EPSC. n = 30 cells from 6 mock-treated mutant mice and 30 cells from 6 HA-CBLN1-treated mutant mice.

(G) PF–PC LTD after rescue. Time course of PF-EPSC amplitudes normalized to baseline and cumulative distribution of LTD magnitude 30 min after induction.

(H) Recovery of hOKR adaptation. Representative traces and mean time course of hOKR gain during training. n = 8 mock-treated mutant mice and 8 HA-CBLN1-treated mutant mice.

(I, J) Recovery of motor and oculomotor phenotypes.

(I) Rotarod latency to fall. n = 5 mock-treated mutant mice and 6 HA-CBLN1-treated mutant mice.

(J) Total spontaneous eye movement distance. n = 6 mock-treated mutant mice and 6 HA-CBLN1-treated mutant mice.

Data are mean ± SEM; dots indicate individual cells or mice, as indicated. *P < 0.05, **P < 0.01,

1114 ***$P < 0.001$. Mann–Whitney U test.

1115 **Table 1 Clinical and molecular features of affected individuals with biallelic variants in**

1116 ***CBLN1***

Family ID	Family 1613		Family 24661
Patient number	**Patient 1**	**Patient 2**	**Patient 3**
Gene	*CBLN1*	*CBLN1*	*CBLN1*
Variant	NM_004352.3: c.335A>G: Tyr112Cys	NM_004352.3: c.335A>G: Tyr112Cys	NM_004352.3: c.187G>C: p.(Ala63Pro)
Zygosity	Homozygous	Homozygous	Homozygous
Ethnicity	Egypt	Egypt	Egypt
Gender	Male	Male	Female
Consanguinity	+	+	+
Family History	+	+	-
Prenatal History	NVD/ irrelevant	NVD/ irrelevant	CS/ irrelevant
Birth weight (kg)	3.5 (-0.1SD)	3.4 (-0.3SD)	3.1(-0.6SD)
Birth length (cm)	50 (-0.06SD)	49 (0.4SD)	48 (-0.6SD)
Birth head circumference (cm)	35 (-0.4SD)	35.5 (-0.18SD)	34.5 (-0.2SD)
Age at last exam	16y	6y	3y2m
Weight (kg/SD)	57 (-0.2SD)	24.5 (+0.9SD)	13 (-0.5SD)
Height (cm/SD)	160 (-1.2SD)	111 (-0.8SD)	90 (-1SD)
HC (Cm/SD)	57.5(+1.67SD)	53 (+1SD)	47.7 (-0.5SD)
Age at first presentation	4m	3m	3m
First presentation	Abnormal eye movement, delayed motor milestones	Abnormal eye movement, delayed motor milestones	Abnormal eye movement, delayed motor milestones
Motor milestones	Sat supported at 1y 8m, sat alone at 3y, stood at 4y, walked supported at 6y, walked steps at 9y, now only 10 steps alone with unsteadiness	Sat supported at 7m, sat alone at 1y, stood supported at 3y, walked supported at 4y, till now couldn't walk alone	Sat supported at 1y6m, sat alone at 2y, stood supported at 2y6m, start to walk supported at last exam with unsteadiness
Mental milestones	First word at 2y, could talk at 5y sentences of 2 words, understand orders	First word at 1y 6m, could talk sentences of 2-3 words, understand and obey orders	Could understand and obey simple orders, first word at 1y 9m, currently could talk 2 words sentences at 3y 2m
Mental development at last exam/ IQ	Could fed himself, currently could know colors, numbers till 300, read simple words and write simple words/ IQ 67	Could fed himself, currently know letters, number and words in shape, could read simple words/ IQ 75	Could know her body parts, single color (red), few shapes, animals and objects/ IQ 74
Seizures	-	-	-
Neuroregression	-	-	-

Behavioral and Psychiatric abnormalities	Laughing without any provocative stimuli	Normal	Normal
sphincteric control	Sphincteric control at 7y both day and night	Sphincteric control at the age of 4y	Not yet (just started)
Dysmorphic facies	Long face, upward slanting palpebral fissures, large prominent triangular nose, smooth philtrum, thin v-shaped upper lip, low set ears	Long face, upward slanting palpebral fissures, smooth philtrum, thin v-shaped upper lip, low set ears	Long face with a pointed chin, high forehead, thin V-shaped upper lip, low set ears
Abnormal eye movement	+/ tonic upward gaze improved with age, squint, horizontal nystagmus, weak movement	+/ tonic upward gaze improved with age, squint, horizontal nystagmus, weak movement	+/ Frequent tonic upward gaze, squint, horizontal nystagmus, weak movement
Squint	+	+	+
dysarthria	+	+	+
Ataxia	+	+	+
Truncal	+	+	+
Appendicular	+	+	+
Intention tremors	+	+	+
dysmetria	+	+	+
Muscle tone	Hypotonia	Hypotonia	Hypotonia
Deep tendon reflexes	Present	Present	Present
Brain MRI	Small cerebellum, mainly the vermis and atrophic, deep white matter signal around the occipital horn, thin corpus callosum	Small cerebellum, mainly the vermis, thin corpus callosum, mild increase extraaxial CSF frontoparietal	Progressive cerebellar atrophy, thin body of corpus callosum
Fundus	Normal	Normal	Normal
VEP and ERG	ERG and VEP: bilateral normal retinal function, bilateral moderate optic nerve dysfunction, bilateral moderate impaired retinocortical transmission	ERG and VEP: bilateral normal retinal function, bilateral moderate optic nerve dysfunction, bilateral moderate impaired retinocortical transmission	ERG and VEP: bilateral normal peripheral retinal function, bilateral moderate macular dysfunction, bilateral moderate optic nerve dysfunction, bilateral impaired retinocortical transmission including occulo- geniculo-occipital transmission
Other findings	Wearing glasses, myope, normal metabolic workup and karyotyping	Wearing glasses, myope, normal metabolic workup and karyotyping	Left hand postaxial polydactyly, Wearing glasses, myope, normal metabolic work up and karyotyping

1117

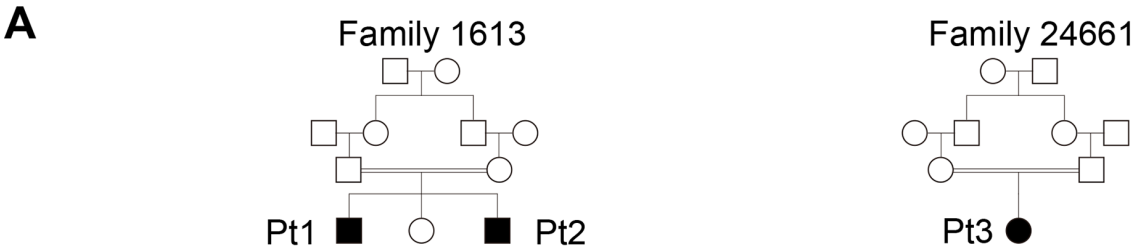

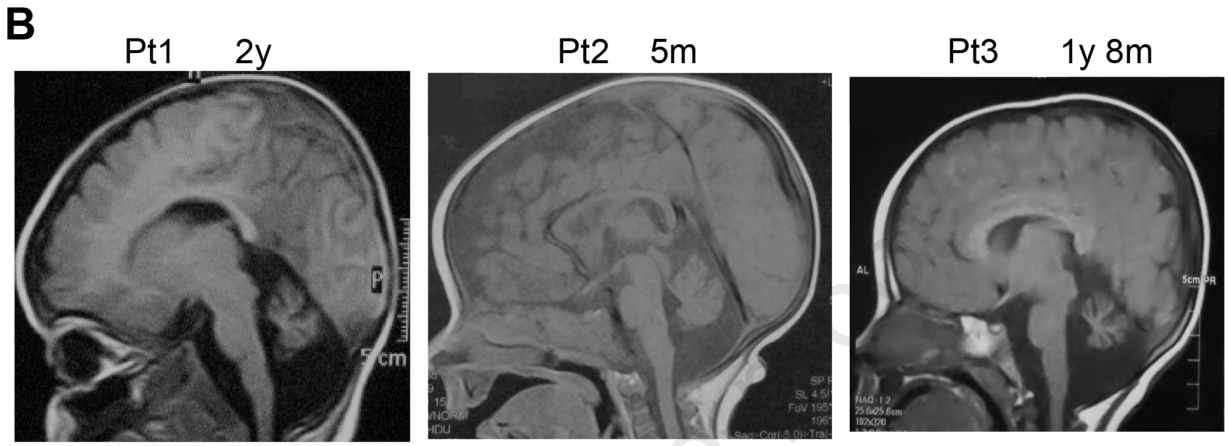

C

Family	Individual	Zygosity	Transcript (RefSeq)	cDNA (HGVS)	Protein (HGVS)
1613	Pt1	Homozygous	NM004352.3	c.335A>G	p.(Tyr112Cys) (Y112C)
1613	Pt2	Homozygous	NM004352.3	c.335A>G	p.(Tyr112Cys) (Y112C)
24661	Pt3	Homozygous	NM004352.3	c.187G>C	p.(Ala63Pro) (A63P)

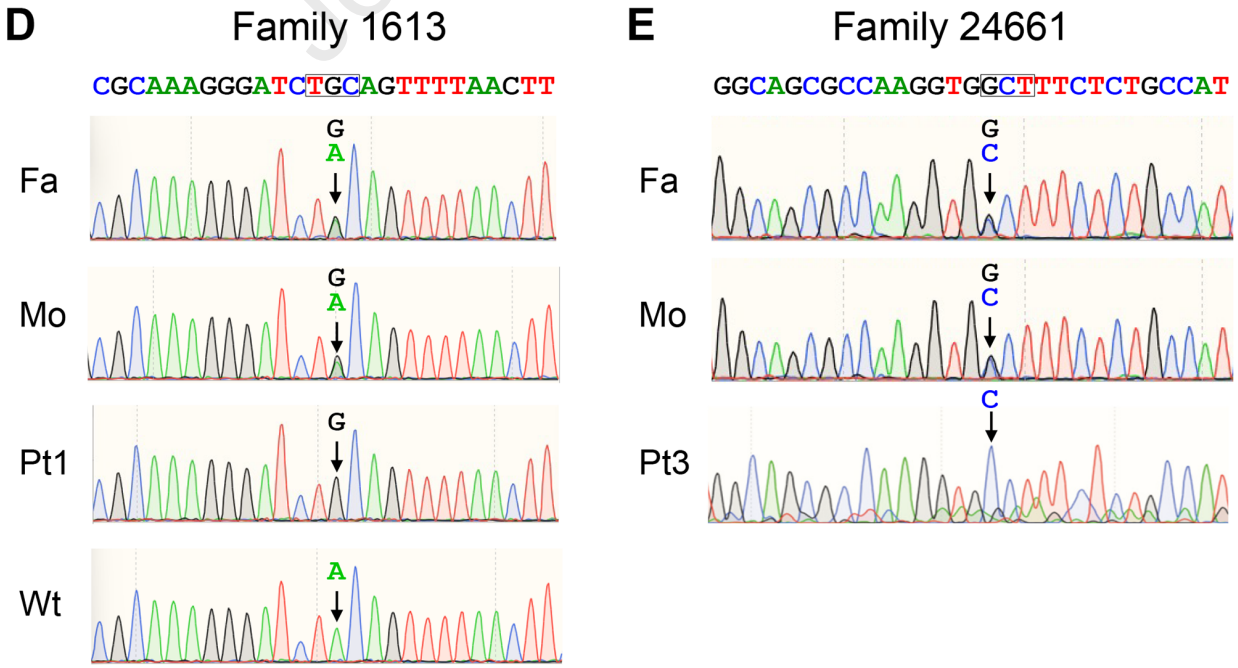

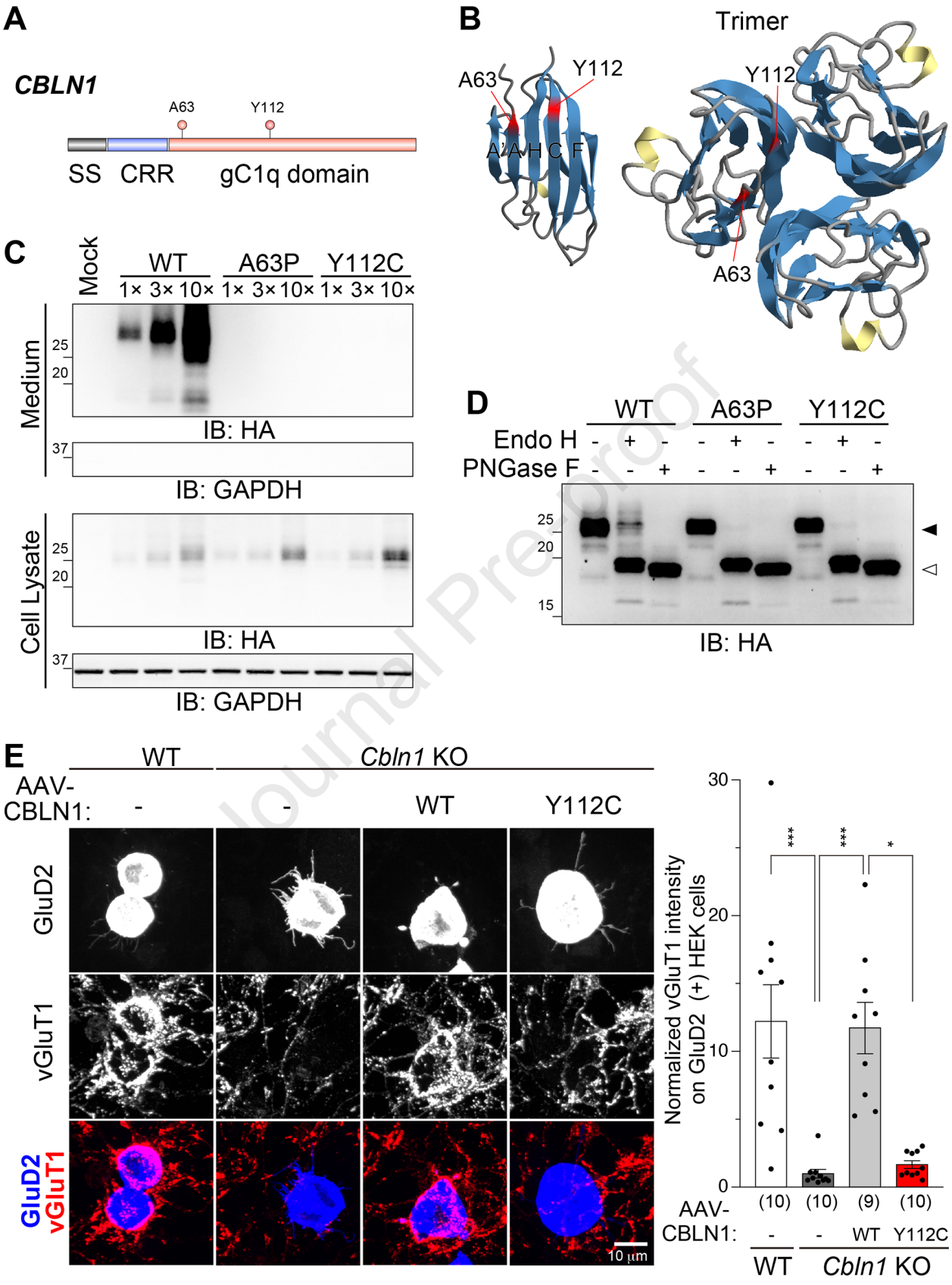

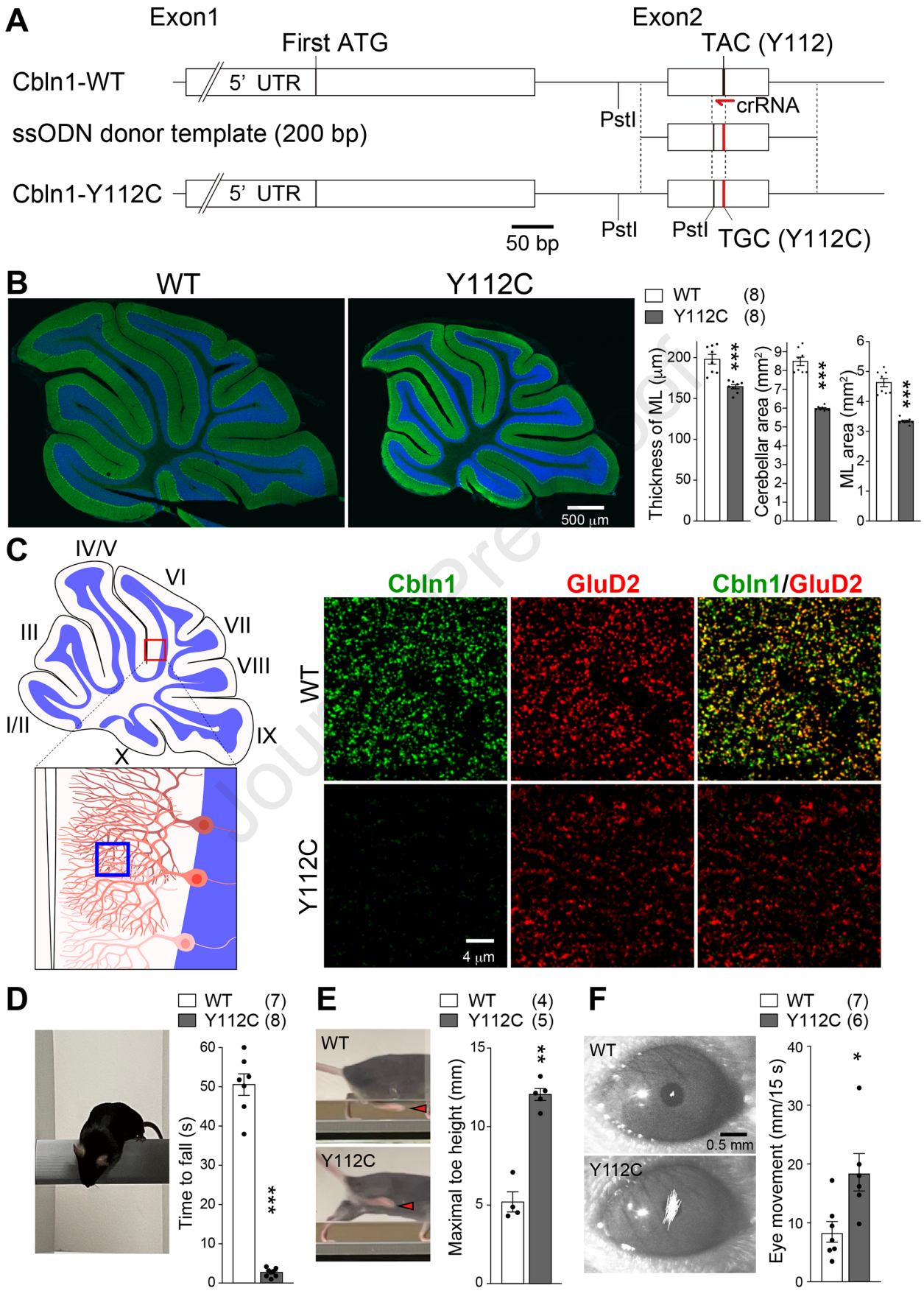
A
Exon1
First ATG
Exon2
TAC (Y112)
Cbln1-WT
5' UTR
crRNA
PstI
ssODN donor template (200 bp)
Cbln1-Y112C
5' UTR
50 bp
PstI
PstI
TGC (Y112C)
B
WT
Y112C
500 μm
WT (8)
Y112C (8)
Thickness of ML (μm)
Cerebellar area (mm²)
ML area (mm²)
***
C
IV/V
VI
III
VII
VIII
I/II
IX
X
Cbln1
GluD2
Cbln1/GluD2
WT
Y112C
4 μm
D
WT (7)
Y112C (8)
Time to fall (s)
***
E
WT (4)
Y112C (5)
WT
Y112C
Maximal toe height (mm)
**
F
WT (7)
Y112C (6)
WT
0.5 mm
Y112C
Eye movement (mm/15 s)
*

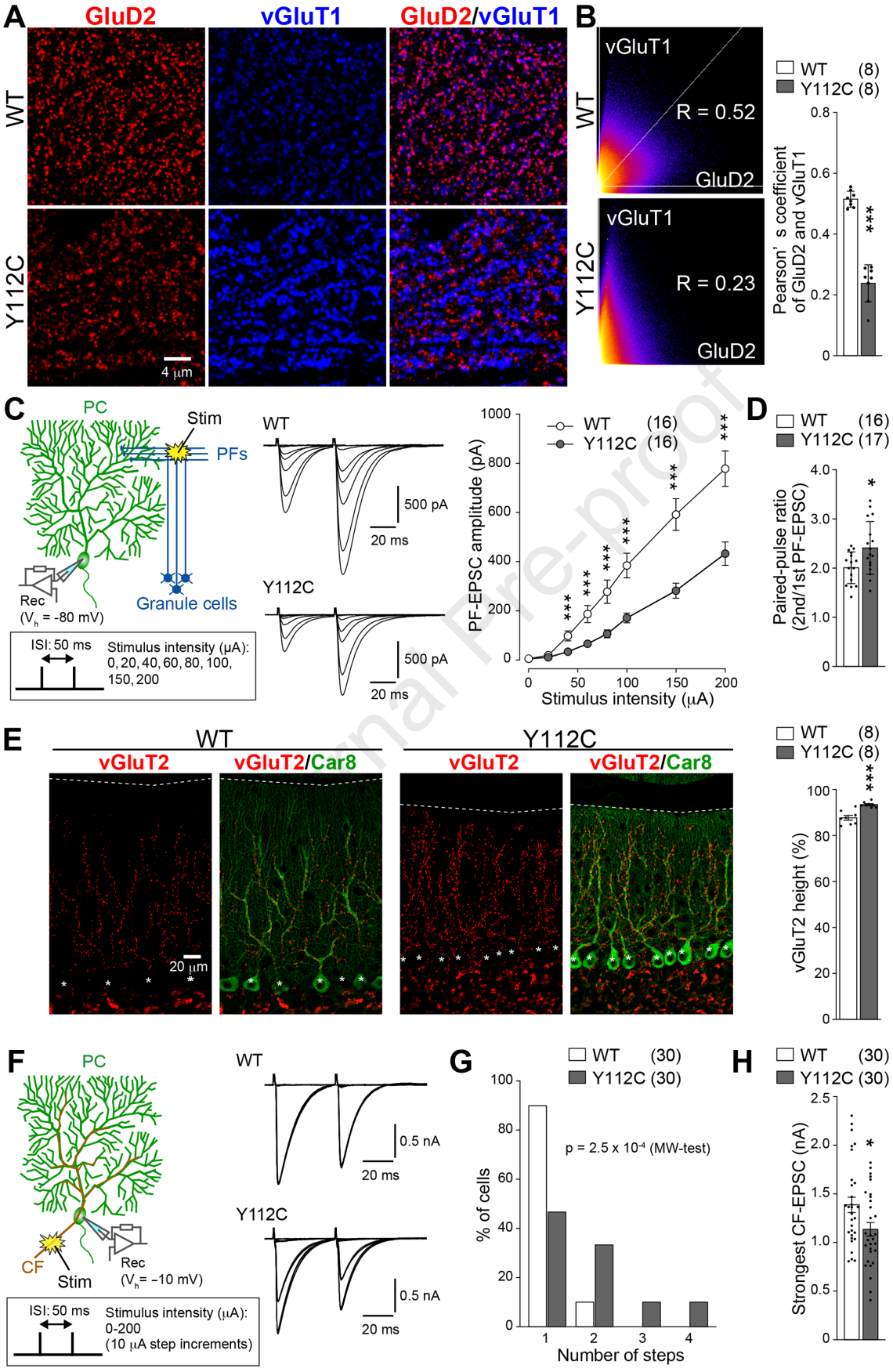
A
GluD2
vGluT1
GluD2/vGluT1
WT
Y112C
4 µm
B
vGluT1
R = 0.52
GluD2
R = 0.23
WT (8)
Y112C (8)
Pearson' s coefficient of GluD2 and vGluT1
***
C
PC
Stim
PFs
Granule cells
Rec
(Vh = -80 mV)
ISI: 50 ms
Stimulus intensity (µA): 0, 20, 40, 60, 80, 100, 150, 200
500 pA
20 ms
PF-EPSC amplitude (pA)
Stimulus intensity (µA)
WT (16)
Y112C (16)
D
WT (16)
Y112C (17)
Paired-pulse ratio (2nd/1st PF-EPSC)
*
E
WT
Y112C
vGluT2
vGluT2/Car8
20 µm
WT (8)
Y112C (8)
vGluT2 height (%)
F
PC
CF
Stim
Rec
(Vh = -10 mV)
ISI: 50 ms
Stimulus intensity (µA): 0-200 (10 µA step increments)
0.5 nA
20 ms
G
WT (30)
Y112C (30)
p = 2.5 x 10-4 (MW-test)
% of cells
Number of steps
H
WT (30)
Y112C (30)
Strongest CF-EPSC (nA)

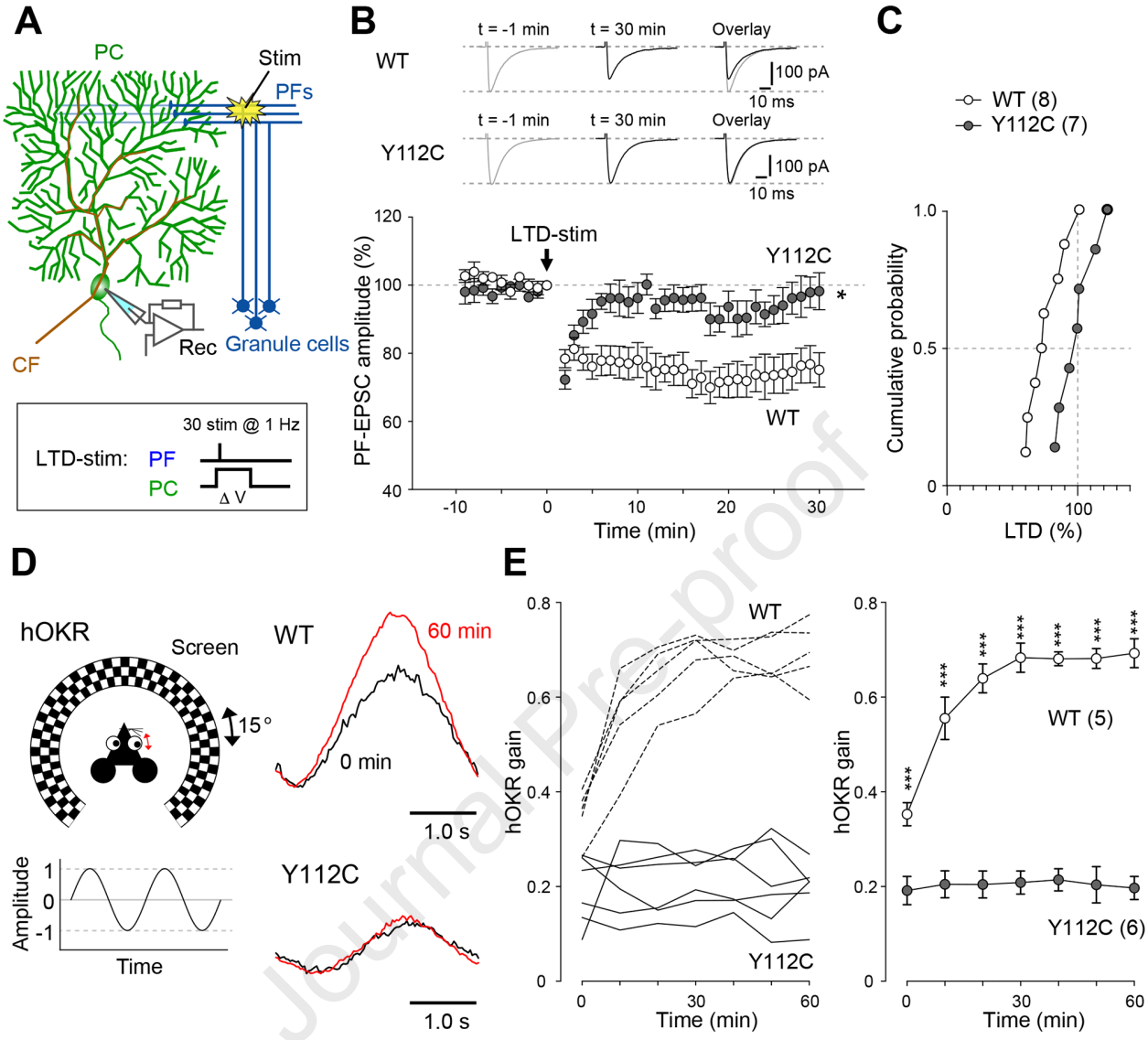

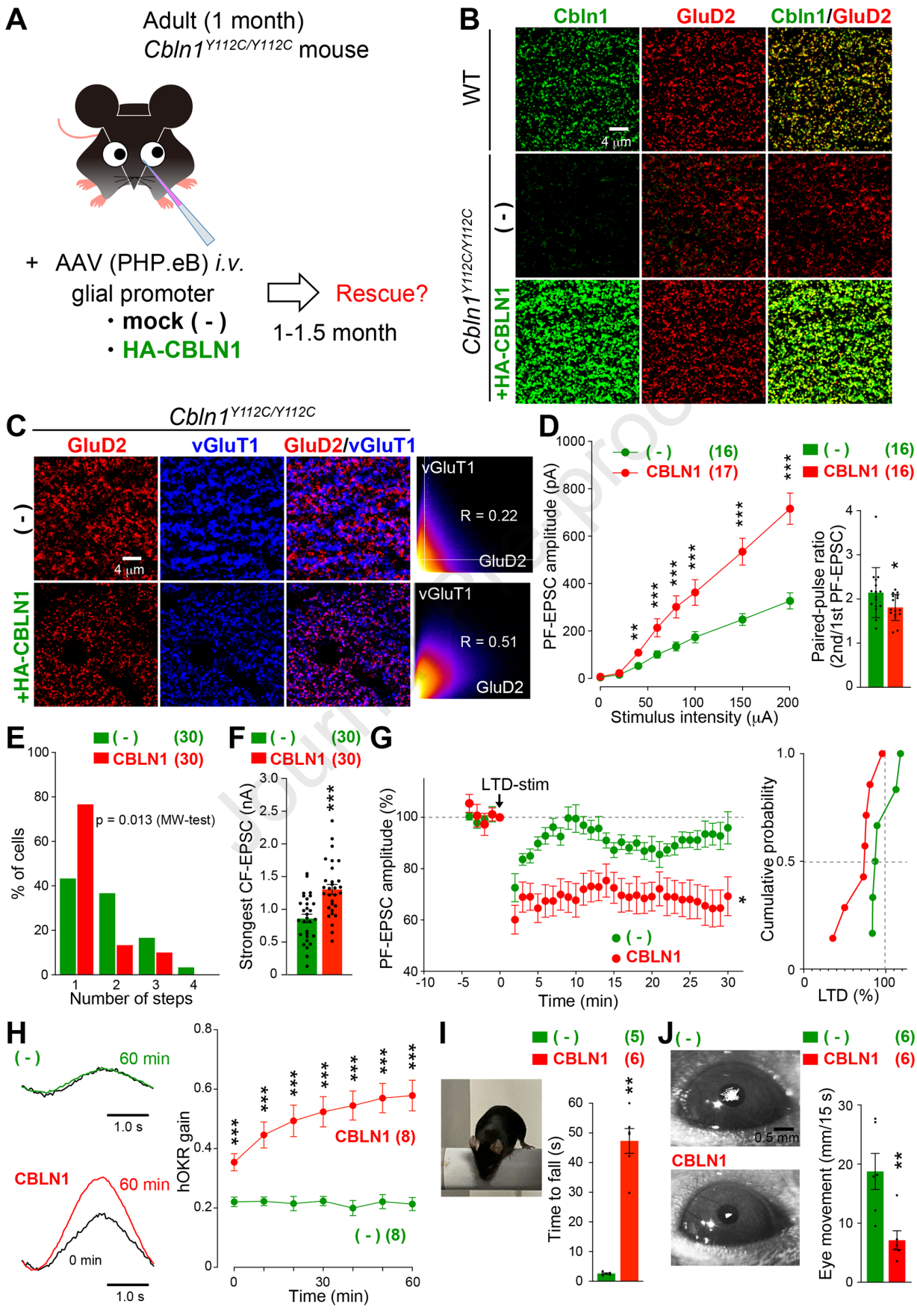
A
Adult (1 month)
Cbln1Y112C/Y112C mouse
+ AAV (PHP.eB) i.v.
glial promoter
• mock (-)
• HA-CBLN1
Rescue?
1-1.5 month
B
Cbln1
GluD2
Cbln1/GluD2
WT
Cbln1Y112C/Y112C
(-)
+HA-CBLN1
4 μm
C
Cbln1Y112C/Y112C
GluD2
vGluT1
GluD2/vGluT1
(-)
+HA-CBLN1
4 μm
vGluT1
R = 0.22
GluD2
vGluT1
R = 0.51
GluD2
D
(-) (16)
CBLN1 (17)
PF-EPSC amplitude (pA)
Stimulus intensity (μA)
(-) (16)
CBLN1 (16)
Paired-pulse ratio (2nd/1st PF-EPSC)
E
(-) (30)
CBLN1 (30)
p = 0.013 (MW-test)
% of cells
Number of steps
F
(-) (30)
CBLN1 (30)
Strongest CF-EPSC (nA)
G
LTD-stim
PF-EPSC amplitude (%)
(-)
CBLN1
Time (min)
Cumulative probability
LTD (%)
H
(-)
60 min
1.0 s
CBLN1
60 min
0 min
1.0 s
hOKR gain
CBLN1 (8)
(-) (8)
Time (min)
I
(-) (5)
CBLN1 (6)
Time to fall (s)
J
(-)
0.5 mm
CBLN1
(-) (6)
CBLN1 (6)
Eye movement (mm/15 s)

Yuzaki and colleagues identify biallelic CBLN1 variants as a cause of early-onset hereditary ataxia and show that loss of extracellular CBLN1 disrupts cerebellar synapses. Astrocyte-targeted AAV delivery restores synaptic CBLN1 and rescues circuit and motor dysfunction, establishing extracellular synaptic organizer replacement as a therapeutic strategy.